The Role of Filamentary Structures in the Formation of Two Dense Cores, L1544 and L694-2

Shinyoung Kim[1,2] , Chang Won Lee[1,2] , Mario Tafalla[3] , Maheswar Gophinathan[4], Paola Caselli[5] , Philip C. Myers[6] ,
Eun Jung Chung[7] , and Shanghuo Li[1]
[1] Korea Astronomy and Space Science Institute, 776 Daedeok-daero Yuseong-gu, Daejeon 34055, Republic of Korea; cwl@kasi.re.kr
[2] University of Science and Technology, 217 Gajeong-ro Yuseong-gu, Daejeon 34113, Republic of Korea
[3] Observatorio Astronómico Nacional (IGN), Alfonso XII 3, Madrid E-28014, Spain
[4] Indian Institute of Astrophysics, 2nd Block, Koramangala, Bengaluru, Karnataka 560034, India
[5] Max-Planck-Institut für Extraterrestrische Physik, Gießenbachstrasse 1, D-85741 Garching bei München, Germany
[6] Center for Astrophysics | Harvard and Smithsonian (CfA), Cambridge, MA 02138, USA
[7] Department of Astronomy and Space Science, Chungnam National University, 99 Daehak-ro, Yuseong-gu, Daejeon 34134, Republic of Korea
Received 2022 April 12; revised 2022 September 20; accepted 2022 September 28; published 2022 November 25

Abstract

We present mapping results of two prestellar cores, L1544 and L694-2, embedded in filamentary clouds in $C^{18}O$ (3–2), ^{13}CO (3–2), ^{12}CO (3–2), HCO^+ (4–3), and $H^{13}CO^+$ (4–3) lines with the James Clerk Maxwell Telescope to examine the role of the filamentary structures in the formation of dense cores in the clouds, with new distance estimates for L1544 (175^{+4}_{-3} pc) and L694-2 (203^{+6}_{-7} pc). From these observations, we found that the nonthermal velocity dispersion of two prestellar cores and their surrounding clouds is smaller than or comparable to the sound speed. This may indicate that the turbulence has already been dissipated for both filaments and cores during their formation time. We also found a $\lambda/4$ shift between the periodic oscillations in the velocity and the column density distributions, implying the possible presence of gravitational core-forming flow motion along the axis of the filament. The mass accretion rates due to these flow motions are estimated to be 2–3 $M_\odot$ Myr^{-1}, being comparable to that for Serpens cloud but much smaller than those for the Hub filaments, cluster, or high-mass forming filaments by 1 or 2 orders of magnitude. From this study, we suggest that the filaments in our targets might be formed from the shock compression of colliding clouds, and then the cores are formed by gravitational fragmentation of the filaments to evolve to the prestellar stage. We conclude that the filamentary structures in the clouds play an important role in the entire process of formation of dense cores and their evolution.

Unified Astronomy Thesaurus concepts: Star formation (1569); Star forming regions (1565); Molecular clouds (1072); Interstellar filaments (842); Interstellar line emission (844); Dust continuum emission (412)

1. Introduction

Dense cores embedded in less-dense large clouds are the birth sites of stars. Since their characteristics represent the initial condition of star formation, the detailed processes of dense core formation and evolution are crucial issues in star formation. A key challenge in the study of core formation is to explain the physical differences between the cores and their natal clouds. While dense cores have a typical size of 0.1 pc diameter and are often spherical in shape, the large-scale clouds in which these cores reside are of a few to tens of parsecs in extent and have irregular shapes (e.g., Bergin & Tafalla 2007; di Francesco et al. 2007). The gas motions in low-mass cores are subsonic and coherent but are more turbulent in the parent cloud (Myers 1983; Goodman et al. 1998).

A number of mechanisms, such as quasi-static contraction via ambipolar diffusion (Shu et al. 1987; Mouschovias 1991) or turbulence dissipation by collisions of supersonic flows (Padoan et al. 2001; Klessen et al. 2005), have been proposed as possible mechanisms for the core formation at the stage prior to the formation of stars, but they do not entirely explain the observational results of the dense cores (Ward-Thompson et al. 2007).

Thus the question of how the dense cores form in the clouds is still under debate.

Recent studies, including the representative Herschel Gould Belt Survey (HGBS; André et al. 2010), have shown that all molecular clouds consist of filamentary structures, and that the majority of gravitationally unstable cores on the verge of star formation, so-called "prestellar cores" (Ward-Thompson et al. 2007), are in locations related to filaments (e.g., André et al. 2010; Könyves et al. 2015), suggesting that dense cores generally form in filamentary cloud structures. In addition, spectroscopic observations of molecular lines have revealed that the large-scale filaments dominated by supersonic motions consist of substructures with a bundle of trans- or subsonic, velocity-coherent, small-scale filaments (a.k.a. "fibers," e.g., Hacar et al. 2013, 2018; Li et al. 2022). Considering the subsonic and coherent characteristics of dense cores and intermediate-size scale of such fibers between the large-scale filaments and cores, their positions in the hierarchical system of the filamentary structure seem to be at the same or lower level of small-scale subfilaments.

A sequential top-down scenario for filament and core formation in such hierarchical filament(-fiber)-core system has been proposed by Tafalla & Hacar (2015). In this scenario, at the earlier stage, turbulent motions in the parent cloud produce a filamentary structure by turbulence dissipation (or a combination of turbulence and gravity; e.g., Padoan et al. 2001; Klessen et al. 2005; Hennebelle 2013) and later the filament is

fragmented into cores by gravitational instability (e.g., Inutsuka & Miyama 1997) and/or magnetic fields (e.g., Fiege & Pudritz 2000a). This scenario is supported by several observational evidences such as the presence of small-scale velocity-coherent subsonic filaments (or fibers), the distribution of cores spaced quasi-equally along the filaments, and the sinusoidal velocity oscillation shifted by $\lambda/4$ for the density fluctuation (see also Hacar & Tafalla 2011; Hacar et al. 2013; Clarke et al. 2016). However, such observational cases are quite limited, and usually the complex filament-fiber system makes it challenging to investigate the velocity structures of individual fibers.

The "isolated" prestellar cores, such as L1544 and L694-2, have been traditionally regarded as the ideal laboratories to study the physical, chemical, and kinematic properties of the evolved starless core and furthermore to investigate the initial condition of star formation (e.g., Lee et al. 2001; Crapsi et al. 2005; Bergin & Tafalla 2007; Keto et al. 2015). In contrast to the recent finding that the majority of gravitationally unstable cores are embedded within the filamentary clouds (e.g., André et al. 2010; Könyves et al. 2015), these isolated cores seem to be rather minority cases in the study of key issues in star formation under the filament paradigm in the sense that their location is well isolated and quite far away from large-scale filaments (e.g., André et al. 2014). Nevertheless, recent high-sensitivity Herschel continuum data show that the clouds around the isolated dense cores are "filamentary-shaped" (e.g., Figure 1). L1544 and L694-2 appear to be isolated filamentary clouds with one core each. Therefore, if these systems are fully velocity coherent, they may represent ideal targets to investigate dense core formation in a filamentary environment with the least influence by other surrounding clouds and their star formation activities.

L1544 is the densest one of three optically selected dense cores (Lee & Myers 1999) in the L1544 dark cloud located in the eastern part of the Taurus molecular complex (Benson & Myers 1989). Its "starless" characteristics were known because of the lack of any far-IR sources detected so far (e.g., Lee & Myers 1999; Figure 1). The L1544 core was identified as the first dense core where gas infalling motions are occurring over the core (Tafalla et al. 1998), and existence of these motions has been confirmed by many subsequent studies with various molecular line observations (e.g., Caselli et al. 1999, 2002a; Ohashi et al. 1999; Williams et al. 1999; Lai & Crutcher 2000; Lee et al. 2001, 2004; Caselli et al. 2012, 2017).

Numerous observational studies of the physical and chemical properties of the L1544 core, such as a high central density of $\gtrsim 10^6$ cm^{-3} (e.g., Tafalla et al. 2002; Keto & Caselli 2010), a severe molecular depletion in core center (e.g., Caselli et al. 1999, 2002a; Tafalla et al. 2002; Young et al. 2004; Kim et al. 2020), and a significant deuterium fraction (e.g., Caselli et al. 1999, 2002b; Hirota et al. 2003; Crapsi et al. 2005, 2007; Redaelli et al. 2019) suggest its highly evolved status.

As shown in Figure 1, the L1544 cloud contains three dense cores of L1544-E, L1544, and L1544-W. The main core L1544 is the largest and densest one, but the other two cores appear to be not dense enough (for example, L1544-E, or L1544-2, was not detected with N$_2$H$^+$ (1–0); Lee & Myers 1999) and are located far from the filamentary cloud. Therefore, in this study, we focus on the main core L1544 only as it is the most evolved and believed to be the most appropriate target in examining the effect of the filamentary structure on the formation of dense core.

L694-2 was first identified in a search for optically selected cores in the L694 small dark cloud (Lee & Myers 1999), and

recognized as a source showing infall motions in molecular line observations by Lee et al. (1999). Since then, L694-2 has been considered a classic case of the infall candidate just like L1544 (e.g., Lee et al. 2001, 2004; Williams et al. 2006; Sohn et al. 2007; Keown et al. 2016). Although L694-2 appears to be relatively less evolved compared to L1544 because of a slightly lower central density or a wider central flat region (Crapsi et al. 2005; Kim et al. 2020), both L1544 and L694-2 cores are believed to be the most evolved prestellar cores on the verge of initiating star formation.

In this paper we present new results from high-resolution mapping observations toward L1544 and L694-2 using the 15 m James Clerk Maxwell Telescope (JCMT) to investigate the kinematics of the dense gas in the cores and their surrounding filaments. The C^{18}O (3–2) line is usually optically thin and traces wider but fairly dense ($\gtrsim 10^4$ cm^{-3}) regions of the filament (André et al. 2007; White et al. 2015). ^{12}CO (3–2) line is a good tracer of infalling motions because it traces less-dense regions surrounding the core and has a high critical density ($> 10^4$ cm^{-3}) and a large optical depth (Lee et al. 2013a; Schneider et al. 2015). Separately, for the purpose of detecting the infalling motions near the innermost region, HCO$^+$ (4–3) and its isotopologue H^{13}CO$^+$ (4–3) lines are selected as optically thick and thin tracers, respectively (Gregersen et al. 1997; Chira et al. 2014). HCO$^+$ and its isotopologues are abundant enough to be detected over prestellar cores (Redaelli et al. 2019; Li et al. 2021), and the $J = 4$–3 transitions have high critical densities ($> 10^6$ cm^{-3}).

In the following sections, using these line observations with complementary dust continuum data obtained from the Herschel science archive, we present the analysis of the physical structures and kinematics of the gas for two prestellar cores, L1544 and L694-2, embedded in filamentary clouds. Sections 2 and 3 describe the JCMT observations, data reductions, the Herschel data, and the results of our observations. Section 4 analyses density structures of the filamentary envelopes of two dense cores and their physical properties. In Section 5, we examine the velocity structures of the filamentary envelopes by considering the Gaussian fit components of the line spectra. Section 6 discusses the radially contracting motions toward the filament and dense core by examining spatial distribution of the asymmetric line profiles. We discuss our results and their implications on the dense core-formation scenario in Section 7, and list our main conclusions in Section 8.

2. Observations

2.1. JCMT-HARP Observations

Observations were carried out toward two dense cores, L1544 and L694-2, with the 15 m JCMT from 2016 July 12 to October 27 (project ID: M16AP025) and from 2017 February 4 to September 16 (M17AP061) under weather conditions with precipitable water vapor (PWV) between 0.83 and 1.58 mm and $\tau_{225\ GHz} \sim 0.05$–0.08.[8]

As for the front-end and the back-end for our observations, we used the Heterodyne Array Receiver Program (HARP; Buckle et al. 2009) and the Auto Correlation Spectral Imaging System (ACSIS). HARP was designed to consist of 4×4 mixers (so-called receptors) in separation of 30″, which make it easier to scan large areas in an efficient way. However, during

---

[8] The conversion from $\tau_{225\ GHz}$ to PWV is given in Dempsey et al. (2013): $\tau_{225\ GHz} = 0.04 \times PWV + 0.017$.
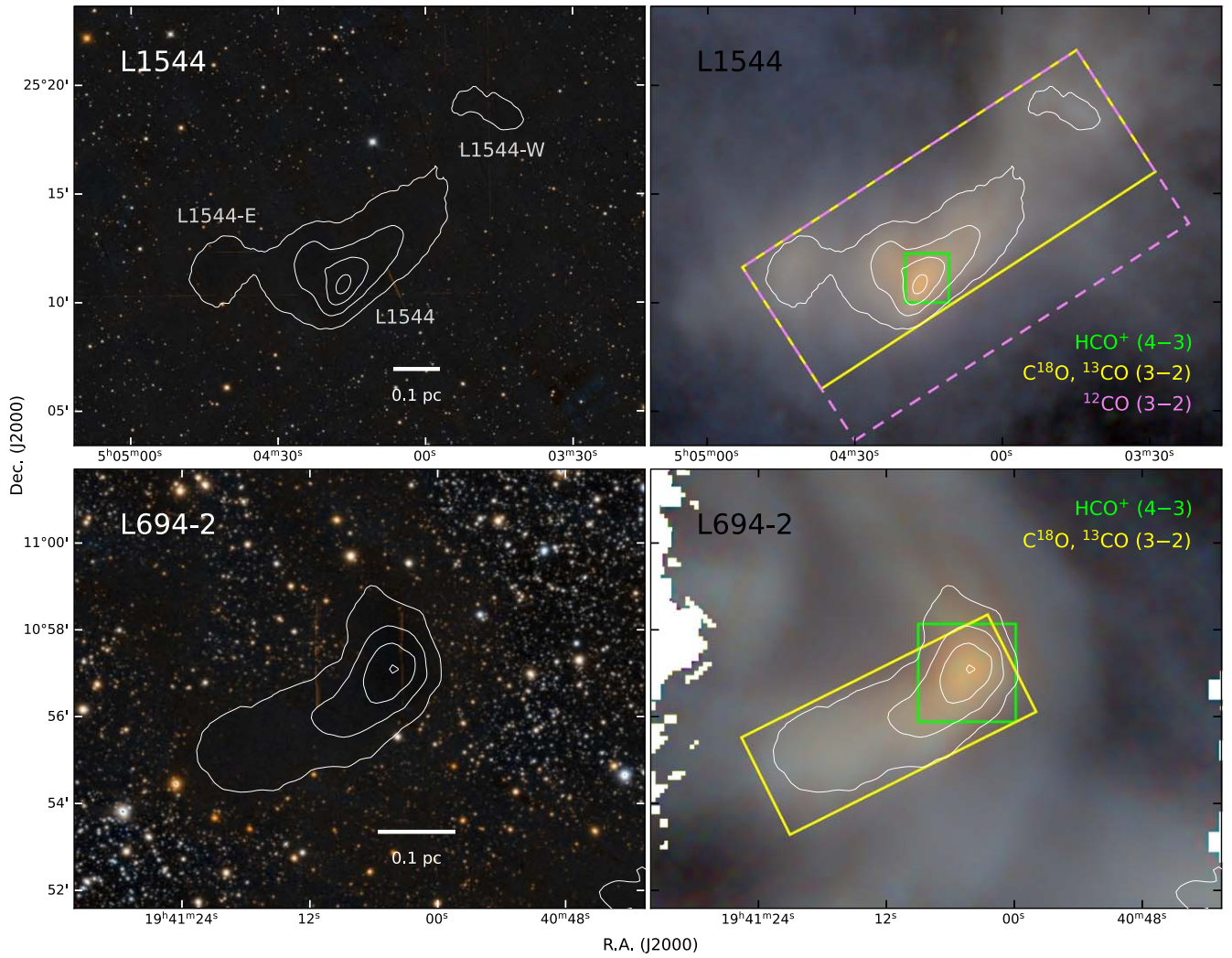
Figure 1. Target cores shown in optical (left panels, Pan-STARRS DR1 color from bands z and g) and far-IR (right panels, Herschel SPIRE color from 250, 350, 500 μm) images. The contours of all panels show the H_2 column densities with levels of 2×10^{21}, 5×10^{21}, 10^{22}, and 2×10^{22} cm^{-2} derived from the spectral energy distribution (SED) fit for Herschel dust continuum data (Figure 5). In the upper-right panel, three dense cores are distinguishable such as L1544-E, L1544, and L1544-W (Tafalla et al. 1998), also referred to as L1544-2, L1544-1, and L1544-3, respectively (Lee & Myers 1999). In this study we only focus on "L1544" and its surrounding cloud. The colored rectangles of the right panels show the mapping areas for each molecular line: lime—HCO^+ and $H^{13}CO^+$ (4–3); yellow—$C^{18}O$, ^{13}CO, and ^{12}CO (3–2); and violet (dashed)—^{12}CO (3–2) for L1544.

our observations, two mixers were not operational, and thus 14 mixers in total were used. The HPBW (half-power beamwidth) at 345 GHz is $\sim 14''$, varying $13''.5$–$14''.7$ depending on the observed frequency. The ACSIS correlator was set to have our required spectral resolutions of $\sim$0.03–0.06 km s^{-1}.

The main molecular lines used for our observations are ^{12}CO (3–2), ^{13}CO (3–2), $C^{18}O$ (3–2), HCO^+ (4–3), and $H^{13}CO^+$ (4–3). While we made a position switching mode observation for the background subtraction, we employed two different mapping modes of "raster" and "grid," for our main targets. The large-scale and relatively low-density filamentary cloud regions were observed using CO isotopologue lines, ^{12}CO (3–2), ^{13}CO (3–2), and $C^{18}O$ (3–2), in the "raster" mapping mode with two spectral windows providing 4096 channels of 61 kHz for a 250 MHz bandwidth, while the central high-density regions of the cores were observed using HCO^+ (4–3) and $H^{13}CO^+$ (4–3) line in the "grid" mapping mode[9] with a

single spectral window providing 8192 channels of 30.5 kHz for the same bandwidth. The molecular lines, their parameters such as the rest frequencies and critical densities, and the achieved frequency and velocity resolutions in our observations are listed in Table 1. The mapped area, the sensitivity achieved for each target, and the corresponding mode employed for the mapping observations are summarized in Table 2.

The raw data were reduced with the ORAC-DR pipeline software (Jenness et al. 2015) with a recipe of "REDU-CE_SCIENCE_NARROWLINE" to produce data cubes of a velocity range ± 10 km s^{-1} centered at the systemic velocity (V_{LSR}) of the source. The reduced data cubes were re-gridded to match one another's pixel grids with a pixel size of $15'' \times 15''$ using hcongrid in FITS_tools,[10] and resampled to have a channel width of 0.06 km s^{-1} for the CO isotopologue lines or 0.03 km s^{-1} for the HCO^+ line using CubicSpline in SciPy (Virtanen et al. 2020). Antenna temperatures (T_A^*) originally given in the data cubes were

---

[9] The data cube consisting of 8×8 pixels with $15''$ spacing was obtained by the stare observations with offsets of (0, 0), ($-15''$, 0), ($-15''$, $15''$), and (0, $-15''$) using the 4×4 array with a beam spacing of $30''$.

[10] https://github.com/keflavich/FITS_tools

Table 1
Observed Molecular Lines and Parameters

Line	$\nu_{\rm rest}$ (GHz)	$\delta\nu$ (kHz)	δv (km s^{-1})	$n_{\rm crit}$ (cm^{-3})
(1)	(2)	(3)	(4)	(5)
^{12}CO (3–2)	345.7959899	61	0.053	1.9×10^4
^{13}CO (3–2)	330.5879653	61	0.055	1.6×10^4
C^{18}O (3–2)	329.3305525	61	0.056	1.6×10^4
HCO$^+$ (4–3)	356.7342230	30.5	0.026	4.0×10^6
H^{13}CO$^+$ (4–3)	346.9983440	30.5	0.026	3.6×10^6

Note. (1) Observed line transitions. (2) Rest frequency of each transition referred from CDMS (Cologne Database for Molecular Spectroscopy; Endres et al. 2016). (3) and (4) Observing spectral resolution in frequency and velocity. In this study, the velocity channels were resampled to 0.06 km s^{-1} (for CO isotopologues) or 0.03 km s^{-1} (for HCO$^+$) for the channel matching between the data cubes. (5) Critical density of lines at 10 K. This was calculated using the equation of $A_u/\sum_{l<u}\gamma_{ul}$ where A_u is the Einstein A coefficient of level u and γ_{ul} is the collision rate out of level u into lower level l at a temperature of 10 K.

converted to the main beam temperatures ($T_{\rm MB}$) using the main beam efficiency ($\eta_{\rm MB}$) of 0.64 (Rawlings 2019).

2.2. Herschel Archival Data

To complement the JCMT observations, we used far-IR dust continuum data observed with the PACS and SPIRE instruments at 160, 250, 350, and 500 μm from the Herschel Space Observatory. The data were taken from the Herschel Science Archive, and their OBSIDs (PI) are 134220484 (P. André HGBS Team 2020) for L1544 and 1342230846 (S. Schnee, HSA 2020) for L694-2. In case of L694-2, there is no PACS observation (160 μm data), but this absence of PACS data is found to have a negligible effect on the spectral energy distribution (SED) fitting result (see Appendix A for details). The L1544 data were obtained as a part of the HGBS (André et al. 2010). The data used here were already zero-point corrected for extended emission based on the cross-calibration with Planck HFI-545 and HFI-857 all-sky maps (Valtchanov 2017). The angular resolutions of 250, 350, and 500 μm images are 18″4, 25″2, and 36″7, respectively. The Herschel images were also re-gridded to match our JCMT observations' pixel grid by the same method as the line data cube (see above section).

3. Results

### 3.1. Parsec-scale CO Emission

Figures 2 and 3 show the intensity maps and the average profiles for 3–2 transitional lines of CO isotopologues, ^{12}CO, ^{13}CO, and, C^{18}O, detected in our JCMT-HARP observations. Our observing lines have rather high critical densities of $1.6–1.9 \times 10^4$ cm^{-3} (Table 1). However, the filamentary structures around both L1544 and L694-2 (or envelopes that are extended widely around the target cores) are found to be well detected over the region traced by the Herschel continuum emission.

$C^{18}O$. The C^{18}O (3–2) emission was detected in regions with H$_2$ column densities $\gtrsim 2 \times 10^{21}$ cm^{-2} (estimated from the dust continuum). The integrated intensity distribution of C^{18}O generally follows the H$_2$ column density distribution well in the filamentary region, although the peak of the C^{18}O emission is slightly offset from the peak position of the H$_2$ column density

distribution in the high-density core region especially in the case of L1544. Most of the line profiles also show a single Gaussian shape, and their velocity positions are consistent with the systemic velocity of each core determined from the previous observation using an optically thin tracer, N$_2$D$^+$ (2–1) (Crapsi et al. 2005). Although there may be effects of slightly high optical depth and/or depletion in C^{18}O (3–2) in the small central region with high-densities, C^{18}O (3–2) is considered an optimal tracer for the kinematics of the filamentary structure around the prestellar core.

^{13}CO. The emission of ^{13}CO (3–2) was detected down to the region where the H$_2$ column density was $\sim 2 \times 10^{20}$ cm^{-2} for L1544 and $\sim 4 \times 10^{19}$ cm^{-2} for L694-2. Similar to the case of C^{18}O, ^{13}CO also traces the high column density region well, but the area over which the line was detected is much wider than that of the C^{18}O covering almost the entire filamentary structure surrounding the core. The ^{13}CO line profiles outside the core region have mostly single-peaked line shapes. Hence, it is easy to measure the velocity of the gas here by making a single-component Gaussian fit even though the peaks are flat due to the high optical depth and do not exactly follow a Gaussian profile. One interesting point to note is that, in the high-density core region of both L1544 and L694-2, the ^{13}CO line profiles show strong self-absorption features (see Section 6 and Figure 11). In L1544, most of the ^{13}CO lines have a double peak and a central absorption dip, while C^{18}O lines show a single Gaussian profile whose peak is located between the two peaks of ^{13}CO. Although there are relatively more profiles with a brighter blue peak (so-called "blue profiles"), about 40% of profiles with comparable blue and red peaks or a brighter red peak are also distributed. However, in the case of L694-2, the blue profiles were predominantly observed. The double-peaked profiles having a clear brighter blue peak or the skewed profiles with a brighter blue peak and a distinct red shoulder were widely found around this core. Therefore, the ^{13}CO line is also considered a useful tracer for the kinematics of both the less-dense part of filamentary structures and the high-density core region.

^{12}CO. The ^{12}CO (3–2) lines were detected on the entire area covered in our observations with H$_2$ column densities down to $2–3 \times 10^{19}$ cm^{-2} in both of the targets. Overall the ^{12}CO spectra in L1544 and L694-2 seem to be highly affected by their high optical depths and thus self-absorbed. There are some differences in these self-absorbed features where ^{12}CO lines in L1544 are more likely double-peaked while those in L694-2 show flat-top shapes, as shown in Figure 3. It is noted that the ^{12}CO emission distribution of L694-2 is significantly distinct from the density distribution. This can be attributed to the presence of two velocity components in L694-2 as shown in the bottom panel of Figure 4, one for the main core of L694-2 and the other for a less-dense part whose systemic velocity is relatively blueshifted with respect to that of the main core by ~ 0.8 km s^{-1}. The velocity maps of L694-2 shown in Figure 4 indicate that the 8.8 km s^{-1} component associated with less-dense parts of the cloud is distributed from east to southeast, crossing the main 9.6 km s^{-1} component of the extended ^{12}CO emission. The original purpose of the ^{12}CO observations was to trace low-density regions surrounding the filamentary structures where the dense cores are embedded, in order to identify any kinematical gas motion toward or along the filaments from low-density diffuse regions. However, contrary to our expectation, the distribution of ^{12}CO emission is quite different from
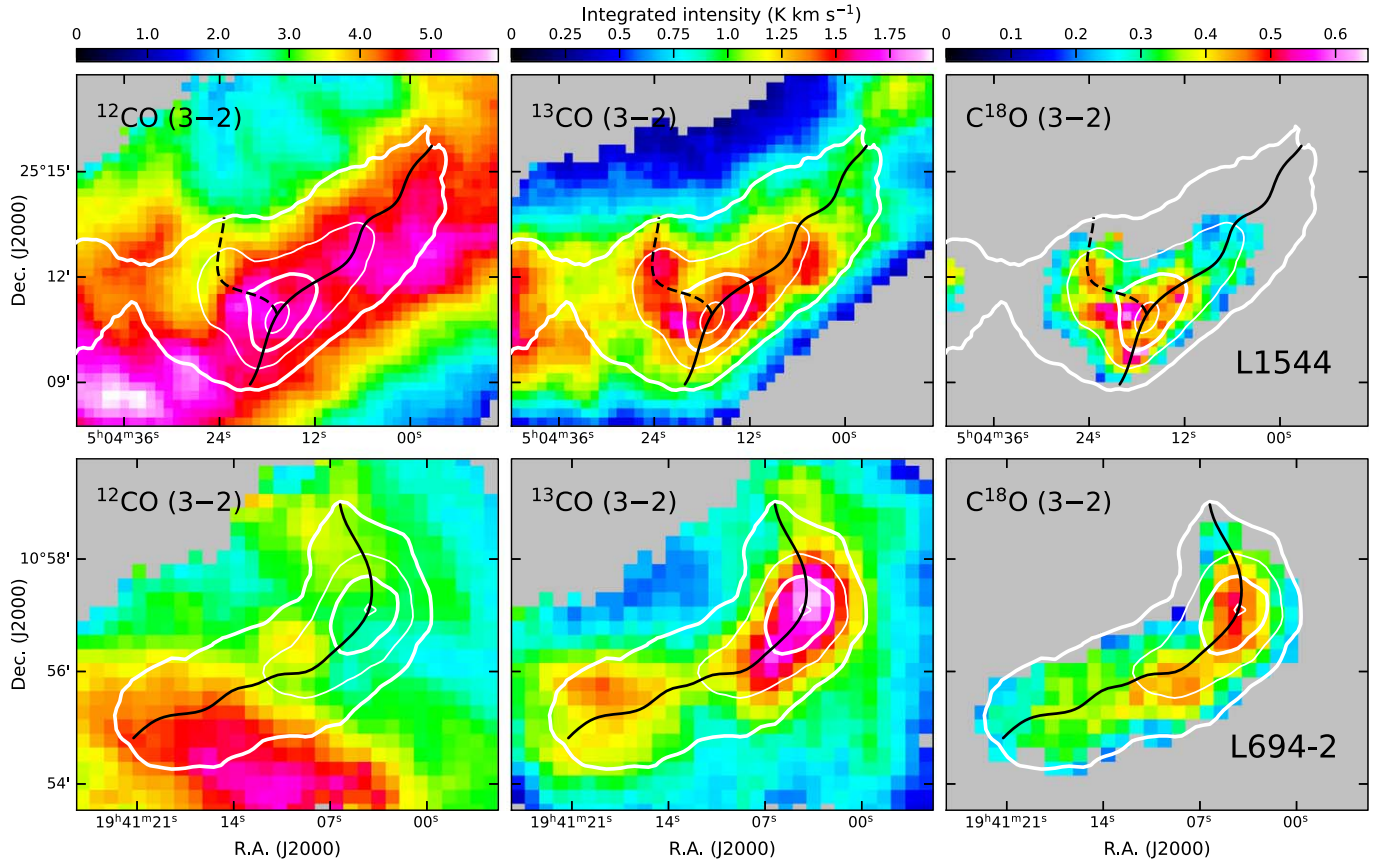
Figure 2. Integrated intensity maps (in color) of ^{12}CO (left panels), ^{13}CO (center panels), and C^{18}O (right panels) emissions for L1544 (upper panels) and L694-2 (lower panels). The white contours show H_2 column densities with levels of 2×10^{21}, 5×10^{21}, 10^{22}, and 2×10^{22} cm^{-2} derived from the SED fit for Herschel dust continuum data (Figure 5). The black solid and dashed lines show the skeletons of filamentary structures (Figure 6).

Table 2
Mapping Areas and Sensitivities

Target	Line	Mapping Area		Mode	σ_{rms}		S/N$_{peak}$	$N_{H_2}^{det}$
		($''$)	(pc)		(K)	(Jy)		(cm^{-2})
(1)	(2)	(3)	(4)	(5)	(6)	(7)	(8)	(9)
L1544	^{12}CO (3–2)	1100 × 570	0.75 × 0.39	R	0.277	8.34	24	$\lesssim 2.7 \times 10^{19}$
	^{13}CO (3–2)	1100 × 400	0.75 × 0.27	R	0.157	4.73	18	2.1×10^{20}
	C^{18}O (3–2)	1100 × 400	0.75 × 0.27	R	0.161	4.85	10	2.5×10^{21}
	HCO$^+$ (4–3)	120 × 135	0.08 × 0.09	G	0.057	1.70	10	6.9×10^{21}
	H^{13}CO$^+$ (4–3)	120 × 120	0.08 × 0.08	G	0.113	3.40	(not detected)	
L694-2	^{12}CO (3–2)	380 × 150	0.37 × 0.15	R	0.348	10.46	17	3.7×10^{19}
	^{13}CO (3–2)	380 × 150	0.37 × 0.15	R	0.175	5.28	23	3.7×10^{19}
	C^{18}O (3–2)	380 × 150	0.37 × 0.15	R	0.139	4.17	10	1.7×10^{21}
	HCO$^+$ (4–3)	135 × 135	0.13 × 0.13	G	0.061	1.83	10	5.6×10^{21}
	H^{13}CO$^+$ (4–3)	120 × 120	0.12 × 0.12	G	0.080	2.39	(not detected)	

Note. (1) Source name. (2) Observed line transition. (3) and (4) Area of the mapping region in units of arcseconds and parsecs, respectively. (5) Observing mode. "R" refers to the "raster" mode, which is the scan mapping with a basket-weave technique a.k.a. the On-The-Fly mapping, and "G" indicates the "grid" mode, which is the mapping mode by the stare observations with the grid spacing. (6) and (7) Mapping sensitivity in kelvin and jansky units with a velocity resolution of 0.06 km s^{-1} (for CO isotopologue lines) or 0.03 km s^{-1} for HCO$^+$ line. The values of the brightness temperature (kelvin) unit were measured in the antenna temperature (T_A^*) scale, and the values of the spectral flux density (janskys) unit were converted using the equation S [Jy] $= 15.6\, T_A^*$ [K]$/\eta_A$ where the aperture efficiency η_A is 0.52 (Rawlings 2019). (8) Signal-to-noise ratio (S/N) at the brightest position of each line. (9) The minimum value of N_{H_2} in the region detected with S/N ~ 3. The ^{12}CO (3–2) line for L1544 was strongly detected in every position, and thus its S/N for the minimum value of N_{H_2} was about 5.4.

those of ^{13}CO and C^{18}O emission, and H_2 column density. This may be because the optical depths of the ^{12}CO lines are high throughout the core and also toward the low-density filamentary region. Indeed the optical depth can significantly reduce

the effective critical density (Shirley 2015). Thus, most of the ^{12}CO lines seem saturated, making it trace only the surface of the filament. Especially for the case of L694-2, the other additional velocity component seems to coexist with the main
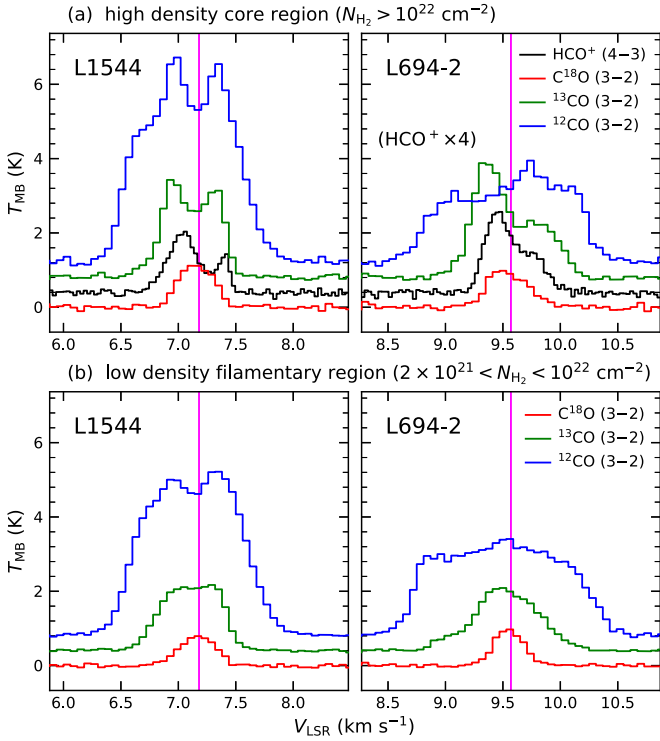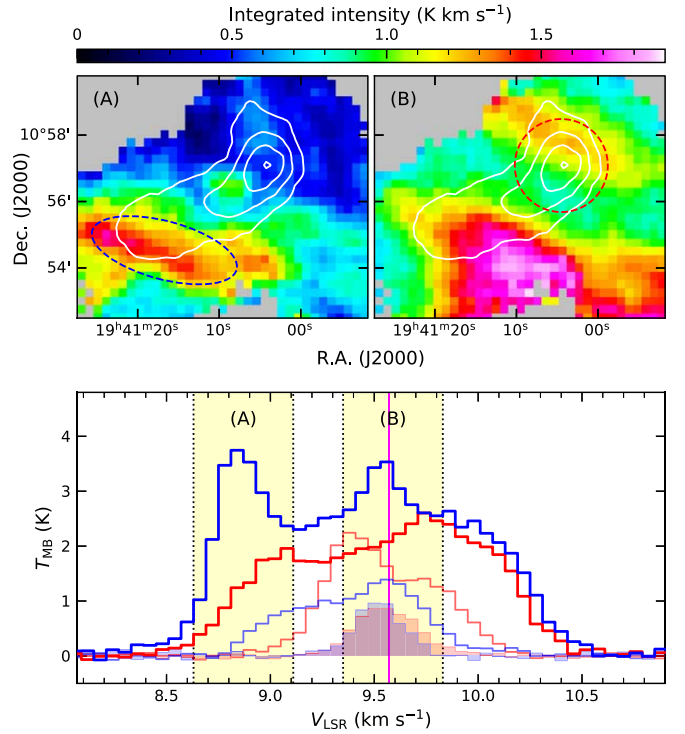
Figure 3. Line profiles of ^{12}CO (3–2) (blue), ^{13}CO (3–2) (green), C^{18}O (3–2) (red), and HCO$^+$ (4–3) (black) emissions for L1544 (left panels) and L694-2 (right panels). The profiles were obtained by averaging the spectra for (a) the high-density core region ($>10^{22}$ cm^{-2}) and (b) the entire filament region ($>2 \times 10^{21}$ cm^{-2}), respectively. The magenta lines show the systemic velocities of target cores derived in Crapsi et al. (2005) using the optically thin tracer, N$_2$D$^+$ (2–1).


Figure 4. Emission distributions (upper panels) and line profiles (lower panel) of CO emissions for two different velocity components in L694-2. The integrated intensity maps were made with a velocity width of 0.48 km s^{-1} and a velocity center of $\sim$8.8 km s^{-1} for (A) and $\sim$9.6 km s^{-1} for (B), which are also displayed in the lower panel with the yellow shaded regions and dotted lines. The line profiles plotted with the blue and red histograms represent the average of the spectra in the regions enclosed with dashed lines of the same colors. Their thick, thin, and filled profiles are for ^{12}CO, ^{13}CO, and C^{18}O, respectively. The magenta line shows the systemic velocity of L694-2.

component. Therefore, our ^{12}CO (3–2) line data appears to be not suitable for determining the kinematics properties of the filaments and the cores. Instead, the ^{13}CO lines are found to have sufficiently strong detection even toward the low-density parts of the filamentary structure with fewer saturation effects. This makes it a good tracer of the overall kinematics of the filaments, and their high-density regions with infall asymmetric profiles that can be used to trace the infalling motion of the outer part of the core or filamentary region.

3.2. Asymmetric HCO$^+$ Emission

The HCO$^+$ line, a well-known tracer of infall motion (e.g., Gregersen et al. 1997; Chira et al. 2014), was selected to track the contracting motion in the innermost region of the core with the high critical density ($\sim$4 × 10^6 cm^{-3}) of the 4–3 transition. As expected, HCO$^+$ (4–3) emission was significantly detected in both L1544 and L694-2 in an extended area with $N_{\rm H_2} \gtrsim 6 \times 10^{21}$ cm^{-2}. In particular, the infall asymmetric profiles were significantly detected with a signal-to-noise ratio (S/N) $\gtrsim$ 10 in the high-density core regions ($>10^{22}$ cm^{-2}) of the two cores as shown in Figure 3, which may allow us to examine the characteristics of the gas kinematics in the cores successfully (Table 2). These infall profiles are found to be distributed over a radius of 0.05 pc from the core center (see Section 6 and Figure 11).

On the other hand, the H^{13}CO$^+$ (4–3) line, which was adopted as an optically thin tracer of infall, was not detected in either L1544 or L694-2. For the detection of H^{13}CO$^+$ (4–3), a noise level of at least $\sim$0.03 K or lower is required, as can be

seen from Table 2. The systemic velocities of the cores were alternatively estimated using N$_2$H$^+$ (3–2) and N$_2$D$^+$ (3–2) data (Crapsi et al. 2005).

4. Density Structures

In this section we analyze the physical structures of the filamentary envelopes of the two cores, especially focusing on the density structures, as they are the basic ingredients to study the kinematics of the cloud cores and their filamentary envelopes.

For this purpose we determined the H$_2$ column density distribution using the Herschel continuum data. According to Section 3.1, the main parts of two filaments are found to consist of a single velocity component. Note that L694-2 has one additional velocity component ("8.8 km s^{-1} component"), but this component traces only the low-density parts of the cloud (as it was not detected in C^{18}O; see Figure 4) and may not have much of an effect on the physical structure of the main filament. Therefore, we should be able to obtain the density structures of the filamentary envelopes using the continuum data. We derived the column density and the dust temperature maps by the iterative SED fitting of the Herschel dust continuum data from 160 (250 for L694-2) to 500 μm using the modified Planck function. In general, we followed the fitting procedure described in Kim et al. (2020). However, there are slight differences compared to the procedure adopted by Kim et al. (2020) in the handling of the continuum data, especially in making the background subtraction and also in adopting
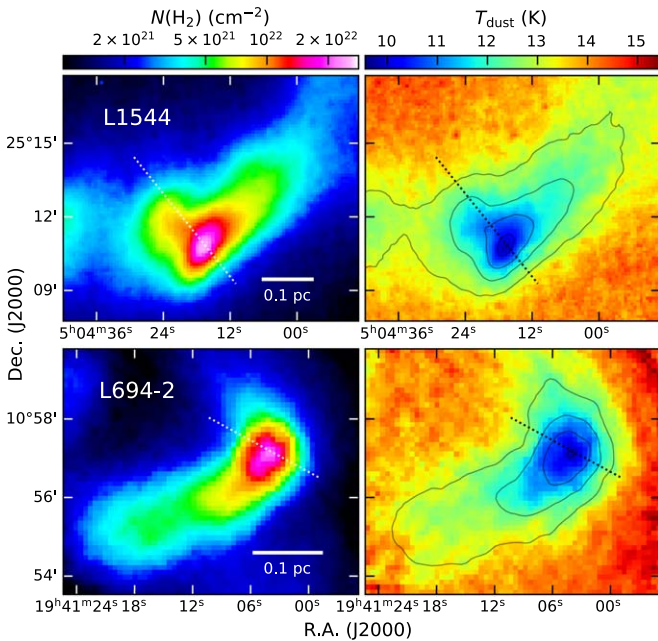
Figure 5. Distribution of column density ($N(H_2)$, left panels) and dust temperature (T_{dust}, right panels) of L1544 (upper panels) and L694-2 (lower panels) derived from the SED fit for Herschel dust continuum data. The dotted lines indicate the positions for which physical properties are displayed as their cut profiles in Figure 15.

optical depth in the equation for the dust emission. These are described in Appendix A.

The resulting distributions of H_2 column density of L1544 and L694-2 including their dust temperature distribution are shown in Figure 5. The H_2 column density maps of the two targets reveal a high-density core and its surrounding filamentary structure of (sub)parsec scale. The high-density core regions show an H_2 column density of $>10^{22}$ cm^{-2} and a dust temperature of 9.5–11 K, while the low-density filament regions show 10^{21}–10^{22} cm^{-2} and 11–13 K. This increasing density and decreasing temperature toward the central dense region in the filaments is typical of starless cores and their envelopes (e.g., Galli et al. 2002; Bergin & Tafalla 2007; Crapsi et al. 2007). Note that the estimated H_2 column densities in the high-density core region are lower than those deduced from millimeter-continuum emission (e.g., Crapsi et al. 2005); however, the far-IR continuum, like Herschel data, is more suitable to trace the dust emissions from the region with a lower density (and necessarily higher temperature), such as a filamentary envelope of core.

4.1. Filamentary Structure

We now find the skeletons of filamentary structures in L1544 and L694-2 using H_2 column density distribution, giving the central axis of filamentary structure or the ridge of density distribution (Figure 6). The skeletons were identified using the `FilFinder`[11] algorithm (Koch & Rosolowsky 2015). For the boundary level of the filament, which is the `FilFinder` parameter for the global threshold, we set an H_2 column density of 2×10^{21} cm^{-2}, which closely matches the 3σ detection level of the C^{18}O emission. Figure 6 shows that L694-2 has a single long skeleton while L1544 has one single main skeleton along
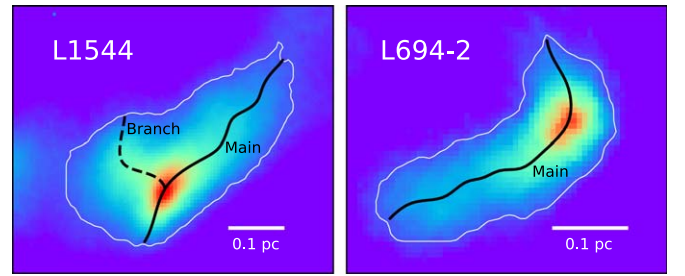
Figure 6. Skeletons of the filamentary structure surrounding L1544 (left panels) and L694-2 (right panels) identified using the `FilFinder` algorithm (Koch & Rosolowsky 2015). The white contour on each panel indicates the filament boundary of an H_2 column density level defined at 2×10^{21} cm^{-2} (see the text for detail).

Table 3
Physical Properties of Identified Filamentary Structures

| Target | Fil. | L | M | M_{lin} |
| | | (pc) | ($M_\odot$) | ($M_\odot$ pc^{-1}) |
(1)	(2)	(3)	(4)	(5)
L1544	Main	0.45	7.1 ± 0.3	15.7 ± 0.6
"	Branch	0.19	3.1 ± 0.1	16.3 ± 0.7
L694-2	Main	0.41	5.0 ± 0.3	12.1 ± 0.8

Note. (1–2) Target and filament name. (3) Projected filament length. (4) Filament mass within the filament boundary level of 2×10^{21} cm^{-2}. (5) Filament mass per unit length (or line mass). Projection effect is not considered.

the main axis of the filament and one small branch skeleton to the northeast, which is emerging out of the core.

4.2. Target Distance

In order to derive physical quantities like the length or mass of the filaments, accurate measurement of the distances of the targets is important. The distance to L1544 is usually considered to be 140 pc with the assumption that the cloud is associated with the Taurus molecular cloud (Elias 1978). The cloud L694-2 is considered to be either at a distance of 250 pc by assuming it to be at the same distance to that of B335, which is located within a few degrees from L694-2 and shows a similar LSR velocity (Lee et al. 2001), or at a distance of 230 ± 30 pc estimated based on the Wolf diagram analysis for the L694 dark cloud containing L694-2 (Kawamura et al. 2001). Thus, it is apparent that the distances to both L1544 and L694-2 are not well constrained.

With the Gaia DR2 astrometric data, more reliable measurements of distance of molecular clouds have been recently made (e.g., Yan et al. 2019; Zucker et al. 2019). However, such reliable estimates of distance are not available for L1544 and L694-2. Therefore, for our study we made an attempt to determine the distances of L1544 and L694-2 using Gaia DR2 astrometric data (Gaia Collaboration 2018) and Pan-STARRS1 stellar photometry. The $g - r$ and $r - i$ colors obtained from the Pan-STARRS1 catalog are used to segregate M-type dwarfs that are lying projected on our target clouds. The extinctions of the M-dwarfs are determined by dereddening the M-dwarfs assuming a normal interstellar extinction law as described in Appendix B. The distances to the identified M-dwarfs are obtained from the Gaia DR2 parallax measurements. We then plotted the extinctions of the M-dwarfs as a function of their
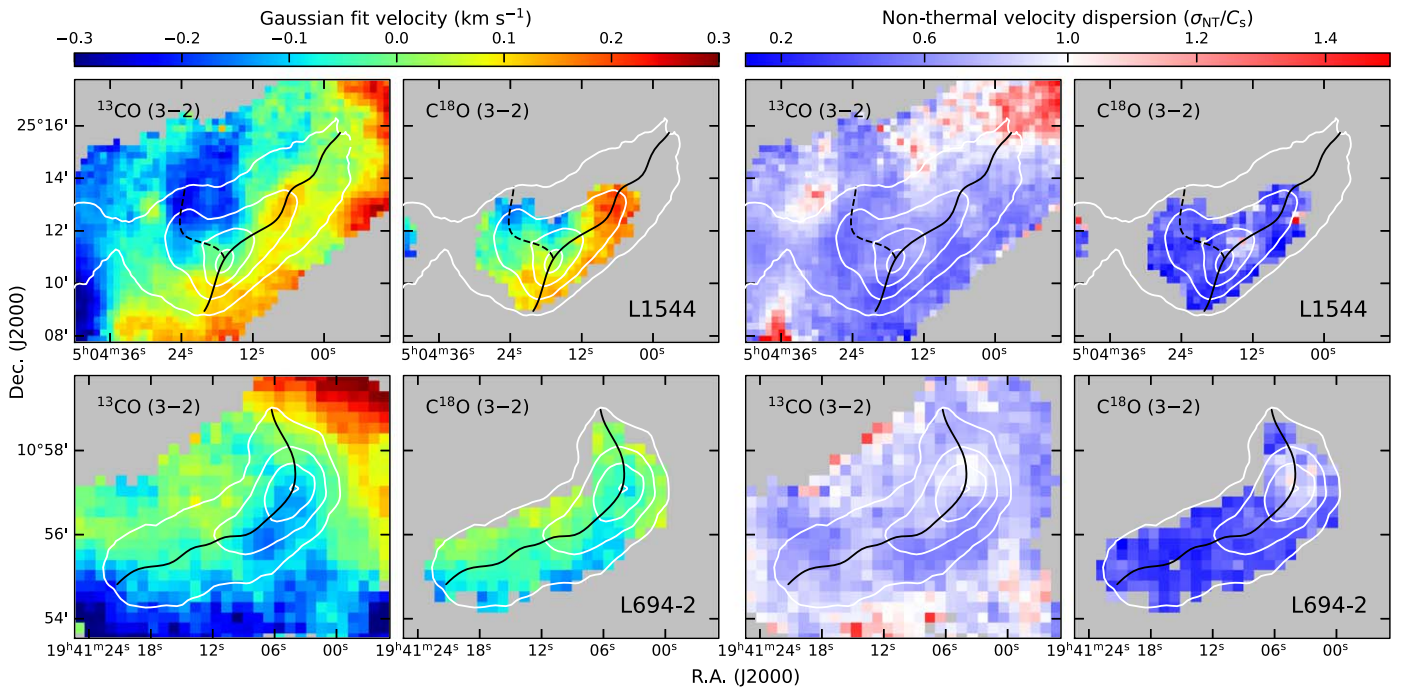
Figure 7. Velocity distributions of L1544 (upper panels) and L694-2 (lower panels) obtained from ^{13}CO and C^{18}O line profiles. Left panels: the distributions of Gaussian fit velocity displayed as the velocity difference from the median velocities (7.12 km s^{-1}) for L1544 and (9.58 km s^{-1}) for L694-2. Right panels: the distributions of nonthermal velocity dispersion expressed by the sonic Mach number (σ_{NT}/c_s). The white contours and the black lines are as described in Figure 2.

distance and determined the distances to the cloud where the extinctions values showed an abrupt increase due to the presence of the cloud. The new distances determined in this way are 175^{+4}_{-3} pc for L1544 and 203^{+6}_{-7} pc for L694-2, which are used for our subsequent analysis. A more detailed explanation of the procedure used to obtain the distance is given in Appendix B.

4.3. Filament Properties

The new distances of the target clouds enabled us to more reliably derive quantities that characterize the physical properties of the identified filaments. These quantities are listed in Table 3. The filament length given in the table is defined as the (projected) length of the skeleton. The mass of the filament is obtained by making a summation of the H$_2$ column densities lying within the contour level of 2×10^{21} cm^{-2}, which is considered as the lowest column density in the filament. For L1544, the 2×10^{21} cm^{-2} contour was not closed due to the existence of another nearby dense core named L1544-E as shown in Figure 1, and thus the filament boundary between L1544 and L1544-E was manually drawn by following the minimum values ($\sim 2.2 \times 10^{21}$ cm^{-2}) between column densities of the two cores (Figure 6). The line mass of the filament, defined as the filament mass divided by the filament length, is given in Table 3 with no correction for its projection effect on the sky.

The mass and size scales of the filaments identified in this study are very similar to those of the filaments found in the L1517 cloud (Hacar & Tafalla 2011) and comparable with those of the velocity-coherent structures, "fibers," which constitute the large-scale filaments in the L1495/B213 region, too (Hacar et al. 2013). These filaments are found to have physical quantities of $L \sim 0.2$–0.7 pc and $M_{lin} \sim 10$–20 $M_\odot$ pc^{-1}. Compared to the mass per unit length (~ 16 $M_\odot$ pc^{-1}) for an

isothermal cylinder at 10 K expected from the models of Stodólkiewicz (1963) and Ostriker (1964), the line masses (M_{lin}) of L1544 and L694-2 filaments are comparable to or less than this critical value, even though these filaments contain the prestellar cores. We note that the M_{lin} might be underestimated by taking a large value of the filament length. In fact most of the mass is concentrated toward the core, while the filament has a long tail of diffuse emission. Therefore, the global M_{lin} may not be the most suitable parameter in characterizing the overall stability of the filamentary clouds. This can be well examined when the M_{lin} is estimated by dividing the main filament into two parts, the core part and tail part, M_{lin}^{core} and M_{lin}^{tail} are 20.7 and 9.8 $M_\odot$ pc^{-1} in L1544 and 16.2 and 8.1 $M_\odot$ pc^{-1} in L694-2, respectively.

5. Velocity Structures

The previous section discusses the density structures by deriving the skeletons of the column density distributions of the two clouds. Now in this section the velocity structures along those density structures are discussed. For this purpose we obtained the velocity centroid and the velocity dispersion for the ^{13}CO and C^{18}O spectra from their Gaussian fits. The velocity distributions that we obtain from these fits are displayed in Figure 7. As mentioned in Section 3.1, most of the C^{18}O spectra have a single Gaussian component with a narrow width, while a significant number of the ^{13}CO spectra often deviate from the Gaussian shape, particularly in the high column density regions where C^{18}O is detected. At the same time, the ^{13}CO spectral shapes get close to a single Gaussian function in the low column density regions where C^{18}O is not detected. Therefore, for the discussion on the velocity structures of our targets along the filaments, we used the velocity information obtained from the C^{18}O spectra wherever it is detected and also
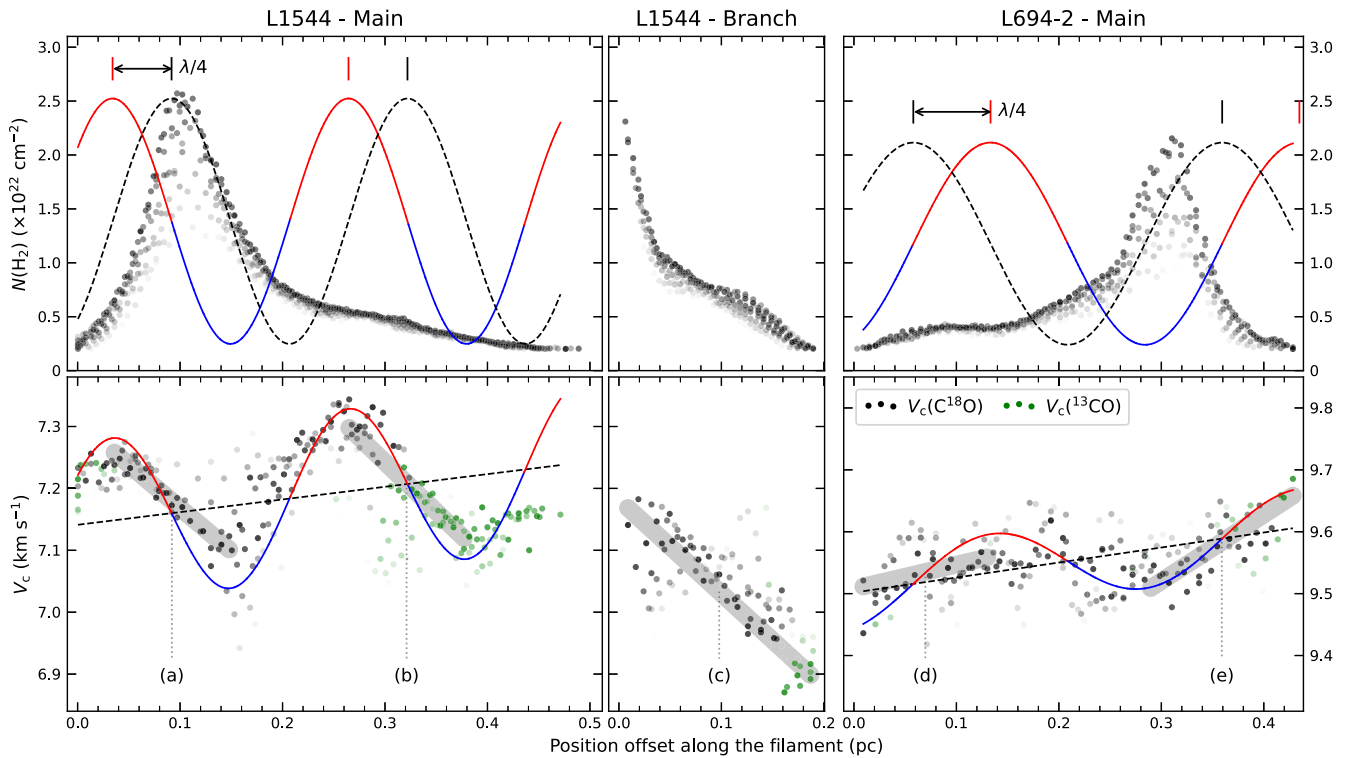
Figure 8. Distribution of velocity centroid and H_2 column density along the filamentary structures in L1544 and L694-2. The *x*-axis is the offset distance in parsecs measured along the skeleton from the southern end of the filament or branch. Lower panels: the black dots represent the $C^{18}O$ velocity centroid and green dots represent ^{13}CO values only for the pixels where $C^{18}O$ is not detected. The data only within a radial distance of 0.15 pc from the skeleton are displayed (the width limit for the plots is 0.3 pc). The red and blue curve is the best sinusoidal fit to the velocity centroid. The black dashed line is a linear gradient in the sinusoidal fit. The gray thick lines are to show the identified local velocity gradients of converging flow motions along the filament listed in Table 4. Upper panels: the black dots represent the H_2 column density. The red and blue curve is a sinusoidal curve with the same frequency and phase values of the best-fit parameters for the velocity centroid, and the black dashed curve is a $\lambda/4$ shifted one. The tone of the dots decreases with radial distance from the skeleton. Designations (a) to (e) indicate the systemic velocities at the points of dense cores where their converging flow motions are measured.

from the ^{13}CO spectra in the low column density region where $C^{18}O$ is not detected.

Overall velocity distributions of two targets obtained using ^{13}CO and $C^{18}O$ line data are shown in Figure 7. A distinct feature in the distribution of the centroid velocities is that there is a clear velocity variation between the filament and its surrounding in both targets. We found large velocity differences of ~ 0.6 km s^{-1} in L1544 and L694-2. This feature is quite similar to synthetic line observations of simulated turbulent clouds (Priestley & Whitworth 2020). The other interesting thing we found is that the nonthermal velocity dispersion is somehow increased at the outer part of the filament. We will discuss implications of these features later in Section 7 regarding the filament formation mechanism. In the velocity distributions, we also found significant variations in the local velocity and velocity dispersion along the filaments, especially around the dense cores. This section will focus on these variations and their possible role in the core-formation process.

5.1. Velocity Variation along the Filament

The velocity variation along the filament can be quantitatively examined with the velocity centroid distribution as a function of distance along the filament's skeleton. The distance of each pixel position along the filament was measured to be the position offset in parsecs measured along the filament's skeleton from the starting point (southern end) of the skeleton. We should note that there are multiple pixel positions along the line perpendicular to the skeleton. They are assumed to have

the same distance as the pixel position along the skeleton. In this way, the velocity variation along the filaments can be displayed as shown in the bottom panels of Figure 8. At the same time, we also derive the H_2 column density distribution along the filaments as shown in the upper panel of Figure 8 that can be compared with the velocity variation along the filaments. We note that in Figure 8 the "branch" filament of L1544 is also indicated as a separate filament structure connecting to the dense core embedded in the filament. Pixels located somewhere between the branch and the main filament were assigned as members of the nearer structure.

The velocity variation and the column density distribution as a function of positions on the filaments measured using the procedure described above and shown in Figure 8 can be used to examine the kinematic structures in a quantitative way. In general, the velocity centroids along the filaments slightly change within a range of 0.3 km s^{-1} or less without a large dispersion, indicating that these filaments are velocity-coherent on the subparsec scale. However, we also note that there are velocity variations at the dense-core-size scale, especially across the dense cores embedded in the filaments. In the case of L1544, such variations are clearly seen over the dense core of L1544 as well as the branch filament of L1544. The branch part of L1544 is in fact directly connected to the dense core of L1544 and thus somehow should be regarded as the boundary part of the dense cores. Similar velocity variation is also seen in L694-2, especially across dense cores of L694-2, although it is less clear than in the case of L1544. These gradients over the

dense cores remind us of the gas flow toward the dense cores related to the core formation in the filament. If the gas flow is somehow associated with the core formation, two velocity peaks would appear with the redshifted and the blueshifted peaks across the dense cores while the velocity at the column density peak position would be close to the systemic velocity of the dense core. This will result in a $\lambda/4$ shift between the velocity and the column density variations where λ is meant to be the wavelength of the variations of the velocity and column density (e.g., Hacar & Tafalla 2011; Liu et al. 2019).

To examine whether such a $\lambda/4$ shift appears in the main filaments of L1544 and L694-2, we performed a sinusoidal fit on the velocity variation using a sine function (Figure 8). The sinusoidal fit was only considered for the data within a radial distance of 0.05 pc from the skeleton and was carried out with the orthogonal distance regression (ODR) using the python package `scipy.odr`.[12] In the fitting process, the results with a wavelength of sine function shorter than 0.1 pc or longer than $2L_{fil}$ (the filament length) were excluded. The L1544 filament shows clear velocity oscillation, which is well fitted to the sine function with a wavelength of ~0.23 pc. In comparison, the velocity oscillation in the L694-2 filament is not as clear as in the case of the L1544 filament, but best fitted with the sine function of a wavelength of ~0.3 pc (lower panel of Figure 8). On the other hand, the density oscillation is not fully seen because each of the L1544 and L694-2 filaments contains only one core. Even though the density oscillation is limited at the scale of the size of the dense core, in the case of L1544, a $\lambda/4$ shift between the velocity oscillation and column density peak is fairly well seen. In the case of L694-2, the phase shift between the velocity and the column density distributions seems slightly larger than the $\lambda/4$ shift. Considering that the density distribution of the dense cores in L1544 and L694-2 filaments is not symmetric along the filaments, this deviation from the $\lambda/4$ shift between density and velocity oscillations does not seem very significant.

Nevertheless, the velocity gradients around the dense cores are more intuitively identifiable, as seen for (a), (c), and (e) in the lower panels of Figure 8, as they are likely the signature of the core-forming flow motion from the filament. The quantitative scale of the core-forming flow motion in filamentary structures can be important in examining the role of filaments in core formation. Following the method of Kirk et al. (2013), the mass accretion rate of the axial flow motion assuming a simple cylindrical model is given by

$$\dot{M}_{\parallel} = \frac{\nabla V_{\parallel} M_{fil}}{\tan \alpha}, \qquad (1)$$

where $\nabla V_{\parallel}$ is the velocity gradient measured along the filament, M_{fil} is the filament mass where the velocity gradient is measured, and α is the angle between the axis of the cylinder and plane of the sky. Local velocity gradients were estimated at five sections indicated by the thick gray lines in Figure 8 and listed in Table 4: two in the main filament of L1544, one in its branch, and two for the filament of L694-2. The sections were separated by the crest to the trough part of the best-fit sinusoidal function, and the data within a radial distance of 0.05 pc from the skeleton were used for the linear fit. These velocity gradients were measured by the linear fit for the data set of the

---

Table 4
Mass Accretion along the Filaments

| #	L_{fil}	M_{fil}	$\nabla V_{\parallel}$	$\dot{M}_{\parallel}$	$\dot{M}_{\parallel,line}$ ($M_{\odot}$ Myr^{-1})
(1)	(pc) (2)	($M_{\odot}$) (3)	(km s^{-1} pc^{-1}) (4)	($M_{\odot}$ Myr^{-1}) (5)	pc^{-1}) (6)
			L1544—Main filament		
a	0.11	2.1 ± 0.1	1.40 ± 0.08	3.0 ± 0.2	26.6 ± 1.9
b	0.11	0.8 ± 0.1	1.59 ± 0.08	1.3 ± 0.1	11.4 ± 0.8
			L1544—Branch		
c	0.18	2.0 ± 0.1	1.52 ± 0.05	3.0 ± 0.2	17.0 ± 0.9
			L694-2—Main filament		
d	0.12	0.7 ± 0.1	0.39 ± 0.06	0.3 ± 0.1	2.2 ± 0.4
e	0.14	1.7 ± 0.1	1.08 ± 0.08	1.8 ± 0.2	13.1 ± 1.4

Note. (1) Position where the converging flows are measured in Figure 8. (2) Filament length along which the velocity gradient is measured. (3) Filament mass within L_{fil}. (4) Velocity gradient measured along the filament. (5) Mass accretion rate of the flow motion along the filament by a simple cylindrical model with $\tan \alpha = 1$. (6) Mass accretion rate per unit length (parsecs) by a simple cylindrical model with $\tan \alpha = 1$.

velocity centroids and position offsets for each filament section so that the slopes given in the fits correspond to the mean values of the velocity gradients for the sections. In L1544, we measured a similar velocity gradient of about 1.5 km s^{-1} pc^{-1} among the core, the branch, and the region of the low-density filament. In the filament of L694-2, its velocity gradients are measured to be 1.1 km s^{-1} pc^{-1} near the core and 0.4 km s^{-1} pc^{-1} for its low-density part. Assuming the inclination angle (α) is 45°, the mass accretion rates near the core are estimated to be 3 $M_{\odot}$ Myr^{-1} for L1544 and ~2 $M_{\odot}$ Myr^{-1} for L694-2, respectively. The extreme case where the α is 0° or 90° can be excluded from the fact that both the filamentary structures do exist and the velocity oscillation along them is significantly measurable. We simply assume $\tan \alpha = 1$ in the later discussion, and our estimated velocity gradients and mass accretion rates are expected to be uncertain by a factor of 2 when the α changes between 30° and 60°.

The mass accretion rate, 2–3 $M_{\odot}$ Myr^{-1}, of the core-forming flow motion is the first quantitative measurement obtained from the sinusoidal velocity oscillations around low-mass prestellar cores and might be the smallest scale among the reported cases of axial mass accretion in the filament so far. The longitudinal accretion rates have been reported as ~10 $M_{\odot}$ Myr^{-1} for the Serpens filament (Gong et al. 2018), 15–35 $M_{\odot}$ Myr^{-1} in the IC 5146 (Chung et al. 2021), and ~45 $M_{\odot}$ Myr^{-1} for the southern filament of Serpens south protocluster (Kirk et al. 2013). In addition, the filamentary flow motions found in high-mass star-forming regions, such as hub filaments, IRDCs, or protoclusters, show 1 or 2 orders of magnitude greater mass accretion rates (Lee et al. 2013b; Peretto et al. 2014; Lu et al. 2018; Yuan et al. 2018). Indeed, all previous cases showing significant differences in accretion scale are not based on the sinusoidal velocity oscillations with the size scale of the low-mass core but the local or global axial velocity gradients of filamentary structures.

The mass accretion rates per unit length of the core-forming flow motions in L1544 and L694-2 are about 11–27 $M_{\odot}$ Myr^{-1} pc^{-1} (Table 4). We note that this amount of the accretion rate is comparable to that estimated from the Serpens filament (~20 $M_{\odot}$ Myr^{-1} pc^{-1}; Gong et al. 2018).
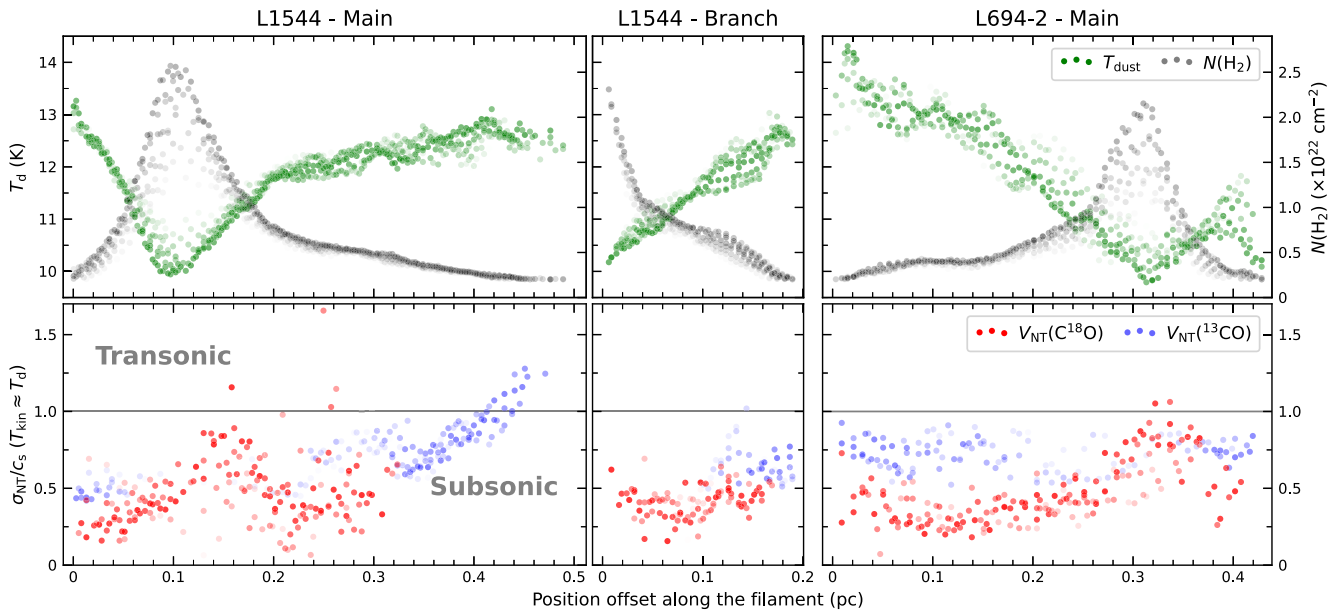
Figure 9. Distribution of nonthermal velocity dispersion as a function of position offset along the filamentary structures in L1544 and L694-2. Lower panels: the red and blue dots represent the nonthermal velocity dispersion in terms of the isothermal sound speed for $C^{18}O$ and ^{13}CO, respectively. The data points brighter than the 3σ level within a radial distance of 0.15 pc from the skeleton are plotted. The ^{13}CO data are corrected for the optical depth broadening and displayed for the positions only with H_2 column density lower than 10% level of the peak value of H_2 column density (see Appendix C). The gray line divides between subsonic and transonic regimes. Upper panels: the black and green dots display the distributions of the H_2 column density and the dust temperature estimated using the Herschel dust continuum data, respectively, in the regions of the core and filament cloud for two targets. The tones of dots are drawn to decrease with radial distance from the skeleton.

5.2. Velocity Dispersion

The observed profile of a molecular line with a certain width is a result of the broadening effects mainly due to thermal and nonthermal motions of the molecular gas. In this section, we examine the characteristics of the nonthermal motion of CO gas in the filamentary cloud. This nonthermal velocity dispersion (σ_{NT}) can be estimated by making a quadrature subtraction of the thermal velocity dispersion (σ_{th}) from the observed velocity dispersion (σ_{obs}):

$$\sigma_{NT} = \sqrt{\sigma_{obs}^2 - \sigma_{th}^2}, \qquad (2)$$

$$\sigma_{th} = \sqrt{\frac{k_B T_{kin}}{m_{obs}}}, \qquad (3)$$

where σ_{obs} is the velocity dispersion (or Gaussian standard deviation) obtained by the Gaussian fit for observed ^{13}CO and $C^{18}O$ spectra, k_B is the Boltzmann constant, T_{kin} is the kinetic temperature, and m_{obs} is the mass of observed molecule. An effect by the σ_{NT} can be expressed by the sonic Mach number ($\mathcal{M} = \sigma_{NT}/c_s$), which is the ratio of the nonthermal dispersion to the isothermal sound speed in a cloud,

$$c_s = \sqrt{\frac{kT_{kin}}{\mu_p m_H}}, \qquad (4)$$

where μ_p is the mean molecular weight per free particle, and m_H is the mass of the hydrogen atom. We used a μ_p of 2.37 obtained with the mass fraction of H: He: Z $\approx$ 0.71: 0.27: 0.02 (Cox & Pilachowski 2000; Kauffmann et al. 2008).

In this study, the optical depth broadening effects for the σ_{obs} values are corrected (details for the correction are described in Appendix C). The ^{13}CO optical depths, $\tau_0(^{13}CO)$, are found to be in a range of about 1–10 in our target regions so that the

optical depth broadening factors, $\beta_\tau(^{13}CO)$, are about 1.18–1.96. The velocity dispersion measured by the Gaussian fit (σ_{fit}) was reduced to the observed velocity dispersion, σ_{obs}, by dividing by these β_τ values.

As for the kinetic temperature (T_{kin}), we adopted the dust temperature, T_d, as its proxy. The T_d all around two target regions are estimated to be in the range of 9.5–14 K. Then the corresponding c_s and the σ_{th} of $C^{18}O$ are calculated to be in the range of 0.18–0.22 km s^{-1} and 0.05–0.06 km s^{-1}, respectively. Note that the σ_{NT} estimation is very sensitive to the values of T_{kin} and τ determined. For example, when $\sigma_{fit} \approx 0.34$ km s^{-1} and $\tau_0 \approx 5$, σ_{obs} becomes 0.2 km s^{-1} if the optical depth broadening is taken into account, and then σ_{NT}/c_s (hereafter Mach number, $\mathcal{M}$) can be quite differently estimated to be 1.06 at 9.5 K or 0.86 at 14 K.

The right panels of Figure 7 show that the nonthermal motions traced by $C^{18}O$ and ^{13}CO are more likely subsonic ($\mathcal{M} \lesssim 1$) in the filament and core regions of both L1544 and L6940-2. Such subsonic characteristics of both $C^{18}O$ and ^{13}CO are also revealed in the distribution of nonthermal velocity dispersion along the filamentary structure as shown in Figure 9. This suggests that the prestellar cores, as well as the surrounding filamentary clouds, seem to be in a quiescent state where the nonthermal gas motions are smaller than or equivalent to the sound speed of the gas. This may be because the turbulence, one of the possible origins for the nonthermal motions, might have dissipated during the formation processes of these quiescent structures (e.g., Myers & Lazarian 1998).

However, although nonthermal motions in the cores and filamentary clouds are within the subsonic regime, it is interesting to note that the amplitudes of the nonthermal motions seem to increase toward the central region of the cores, being almost transonic (Figure 9). Since $C^{18}O$ only traces the outer region of the core, unlike high-density tracers, this increase in
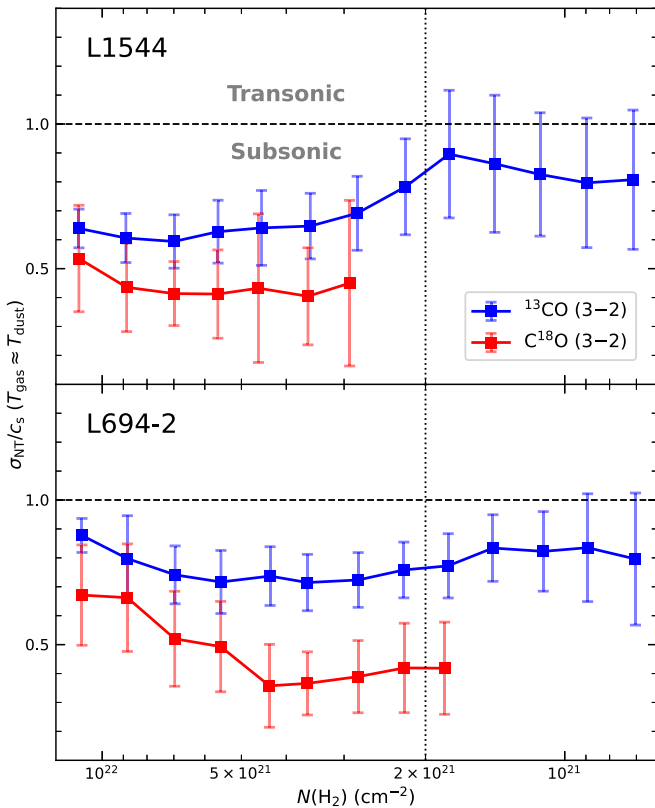
Figure 10. Nonthermal velocity dispersion (expressed by the sonic Mach number) obtained from ^{13}CO (blue) and C^{18}O (red) spectra vs. H$_2$ column density in L1544 (upper panel) and L694-2 (lower panel). The dashed horizontal line divides the subsonic and transonic regimes, and the dotted vertical line indicates the filament boundary.

nonthermal motions at the core region may be related to the gas motion in the less-dense region moving toward the core region such as the core-forming flow discussed in the previous section or the radial infall to be discussed in the next section. A similar increment of velocity dispersion toward the core has been also found in the SDC13 cores, which is suggested to be purely generated by gravity (Williams et al. 2018). We also see a gradual increase of nonthermal motions to the transonic regime at the northwest end of the L1544 main filament, the region traced by the ^{13}CO line. This is probably because the region is highly affected by the gas flow motions, as shown in Figures 7 and 8.

In addition to the northwest part of L1544, the σ_{NT}(^{13}CO) is slightly increased outside the filament compared to the inner part. Figure 10 shows the σ_{NT} variation of ^{13}CO and C^{18}O with respect to the H$_2$ column density to examine the reliability of this increase. The σ_{NT} data points plotted in Figure 10 are averaged values along the isocontour of H$_2$ column density. Although the averaged σ_{NT} lies in the subsonic regime over the entire density range, there are slight increases of σ_{NT}(^{13}CO) from the inside to the outside of the filament boundary. In particular, the steep increase ($\Delta\sigma_{NT}$(^{13}CO) $\sim 0.25c_s \approx 0.06$ km s^{-1}) in L1544 is significant.

Pineda et al. (2010) also found a sharp increase of the velocity dispersion in the B5 region of Perseus from subsonic to transonic across the filament boundary using a single tracer, NH$_3$ (1, 1) emission. In our target, such variation in σ_{NT}(^{13}CO) between the inner and outer regions of the filament is less prominent than that shown in the B5 region.

Note that recently Choudhury et al. (2021) found from NH$_3$ (1, 1) and (2, 2) observations of L1688 that there is a less sharp transition to coherence with $T_{kin} \lesssim T_{dust}$ (Herschel-based) in the dense core and $T_{kin} \gtrsim T_{dust}$ in the cloud. Thus, if this is the case for L1544, then the thermal contribution might be over-estimated inside and underestimated outside, and therefore such an increase in σ_{NT}(^{13}CO) toward outside the filament can be even less than that shown here.

6. Infall Motions

In Section 5.1, we found that a significant gas flow into the dense cores is in the form of oscillating motions along the filamentary envelopes. Therefore, it may be possible that such gas flow may affect the growth of the embedded cores. One way for checking this growth would be to look at the gas infalling motions around the dense cores. In this section we examine the radially contracting motion toward the core or the filament by observing the infall signatures in the molecular lines, a feature of "infall asymmetry" in the self-absorbed spectra (e.g., Lee & Myers 1999; Lee et al. 2001).

Figure 11 shows a host of infall asymmetries in the HCO$^+$ (4–3) and ^{13}CO (3–2) line profiles around the core region. We refer to these profiles showing infall asymmetry as the "blue profile" in this paper. The blue profile was identified by comparing the brightness temperatures of the blue peak (T_b) and the red peak (or shoulder) (T_r) measured by double Gaussian fitting for each line profiles. Figure 12 shows the statistics for the following three cases based on the rms noise level (σ) of the line: (1) brighter blue peak than red peak ($T_b - T_r > \sigma$), (2) comparable blue and red peaks ($|T_b - T_r| < \sigma$), and (3) brighter red peak ($T_b - T_r < -\sigma$). Most of the HCO$^+$ (4–3) and ^{13}CO (3–2) line profiles in L694-2 display blue asymmetry. In the case of L1544, 38% of ^{13}CO and 14% of HCO$^+$ spectra have shapes with comparable or brighter red peak, but the majority of the line profiles are classified as blue profiles.

6.1. Infall Motions in Core Region

As mentioned above, both ^{13}CO (3–2) and HCO$^+$ (4–3) lines around the core region show strong self-absorption features, mostly seen as the blue profile. Considering that these two tracers have different critical densities by 2 orders of magnitude, they likely trace different density regimes. Thus, the dominance of the blue profiles in both ^{13}CO and HCO$^+$ lines around the core region may indicate that the gaseous material in both the surrounding envelope and the innermost region of the core is infalling in a similar fashion onto the core center. Note that this is consistent with recent findings from Ching et al. (2022) for L1544. In particular, the agreement in infalling signatures in both molecular lines is remarkable in L694-2, implying that the core L694-2 is experiencing the contracting motions in its entire region. On the other hand, we note that the ^{13}CO line data in L1544 show some small portion of red asymmetric profiles (hereafter the red profile), indicating that there may be some other complicated motions in the low-density outer envelope of L1544 such as expansion, or oscillation, probably due to some possible inflowing motions along filaments. Because of this complex pattern of the profiles in the envelope of L1544 core, we discuss infalling motions in the central region of L1544 core using HCO$^+$ lines only.

The line profiles of HCO$^+$ and ^{13}CO shown in Figure 13 are the average of the profiles within the 40% level (p_{40}) contour of
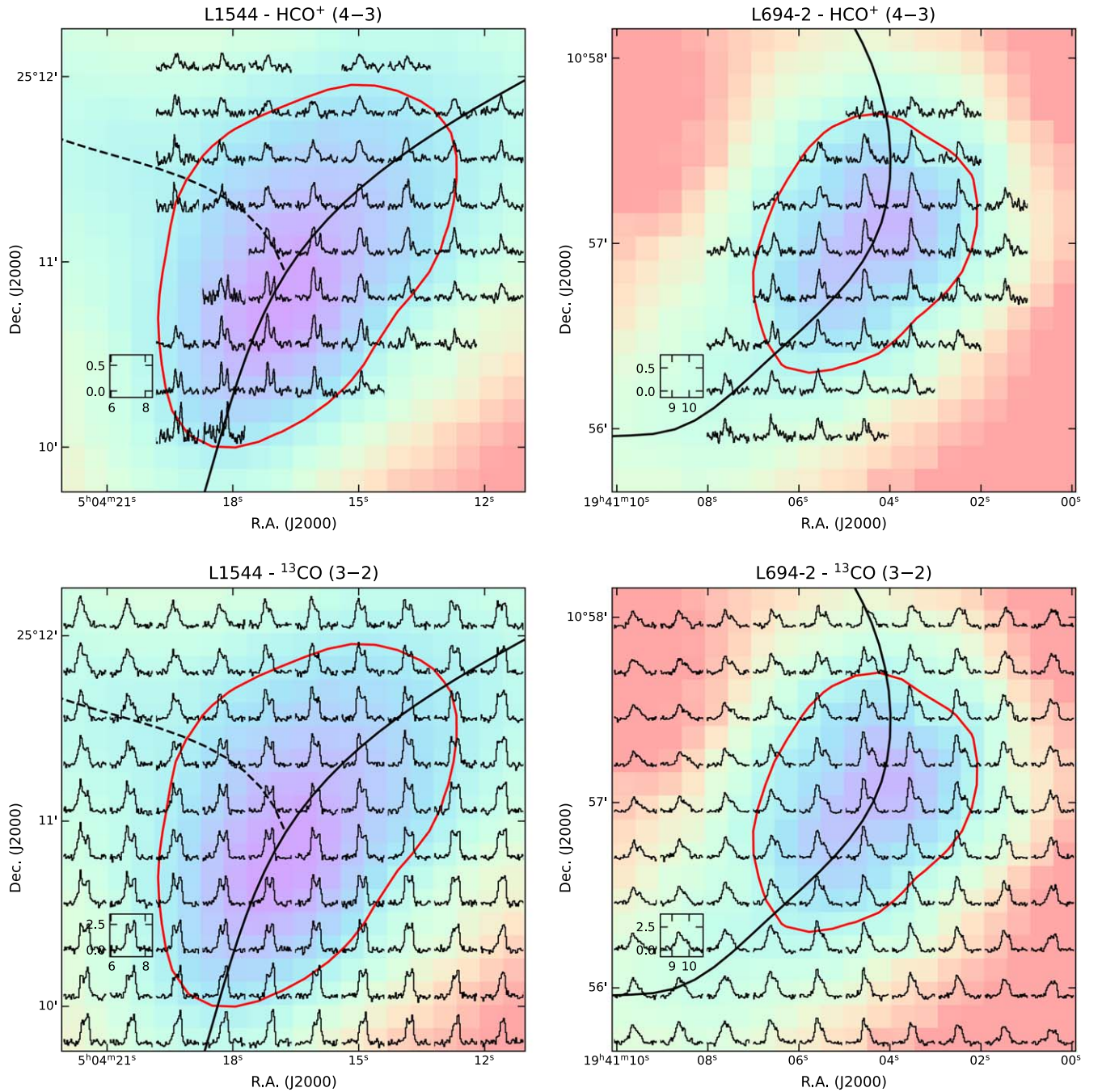
Figure 11. Line profile maps of HCO^+ (4–3) and ^{13}CO (3–2) lines for L1544 and L694-2. The background color indicates the H_2 column density distribution. The red contour in each panel is to display the 40% level of its peak value (p_{40}). The skeleton of filamentary structure is shown by the black solid or dashed lines.

the H_2 column density peak of each dense core (the red contours in Figure 11). We used the 40% level contour in our analysis rather than a half-maximum contour generally used, as the 40% level contour was found to be more useful in this study to include a sufficient number of the blue profiles to cover the whole infalling central region and also to obtain an average profile with a sufficient S/N, which will enable us to make a better fit to the infall model. These average line profiles were used to analyze infall velocities and mass infall rates toward the cores. The infall velocity of the average profile was determined by fitting the profiles with the Hill5 infall model (De Vries & Myers 2005). This Hill5 model is a simple radiative transfer model used for deriving infall speeds in a contracting molecular

cloud by dealing with radiative transfer processes in two approaching layers whose excitation temperatures linearly increase toward the inner region. Based on the error analysis for the Hill5 model, De Vries & Myers (2005) suggested that an S/N greater than ∼30 is usually required to reliably determine the infall velocity from the asymmetric line profile shape. In this study, we used a spectrum with an S/N of at least 25 for fitting it with the Hill5 model. The fitting was performed by Markov Chain Monte Carlo (MCMC) sampling using the emcee[13] python package (Foreman-Mackey et al. 2013) to

---

[13] https://github.com/dfm/emcee
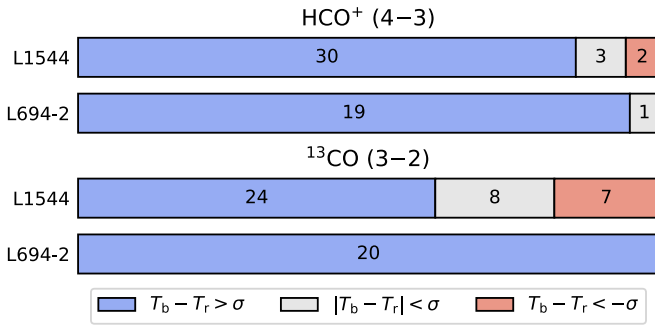
Figure 12. Number statistics of the blue and red profiles in ^{13}CO and HCO$^+$ lines within the 40% contour of the peak value of the H$_2$ column density at the core center for two dense cores, L1544 and L694-2. T_b and T_r are the brightness temperatures of the blue peak and the red peak (or shoulder) measured by double Gaussian fitting for each line profile, and σ is the rms noise level of each line profile.

ensure the reliability of the fitting result and accurately estimate the error. The best-fit profiles are over-plotted on the averaged line profiles in Figure 13. The resulting infall velocities from the fit are about 0.1 km s^{-1} in all three cases, as listed in Table 5. Note that the infall velocity of 0.1 km s^{-1} is very close to that found by Keto & Caselli (2010) in L1544, at a distance of about 1000 au, where the volume density is about 10^6 cm^{-3}.

These infall velocities can be used to derive the mass infall rate of gaseous material incoming toward the core center through the surface of the infall radius by an equation as follows (e.g., Lee et al. 2001):

$$\dot{M}_{in} = 4\pi R_{in}^2 \rho V_{in}, \qquad (5)$$

where R_{in} is the radius of the region showing infall motion (hereafter, infall radius), ρ is the density of the infalling shell, and V_{in} is the infall velocity. In this approach, we assume that the infall motions are spherically symmetric toward the center of the cores. Assuming the core has a spherical shape with uniform density, ρ, within the infall radius, its density is given by

$$\rho = \frac{3M_{in}}{4\pi R_{in}^3}, \qquad (6)$$

where M_{in} is the total mass in the region within R_{in}, and thus, the mass infall rate can be expressed by

$$\dot{M}_{in} = \frac{3M_{in}}{R_{in}} V_{in}. \qquad (7)$$

The mass infall rates estimated from the HCO$^+$ line profile are $\sim$16 $M_\odot$ Myr^{-1} for L1544 and $\sim$13 $M_\odot$ Myr^{-1} for L694-2 (Table 5). We have assumed R_{in} to be r_{40}, the radius of a circle embracing the same area as the area within the p_{40} level contour. M_{in} was obtained from the sum of H$_2$ column densities inside the p_{40} contour. Since there is a flat density region in the prestellar core center to a radius of about 0.02–0.05 pc (Kim et al. 2020), this approximation is thought to be fairly reasonable with HCO$^+$ line data, but may not be so with ^{13}CO data, which would trace the much-less-dense outer region. The blue profiles in ^{13}CO are spatially more extended than the HCO$^+$ cases and are seen even down to the region of $\sim$10% level of the peak column density value (p_{10}). Thus, using r_{10} as infall radius in the case of ^{13}CO data may be more reasonable.
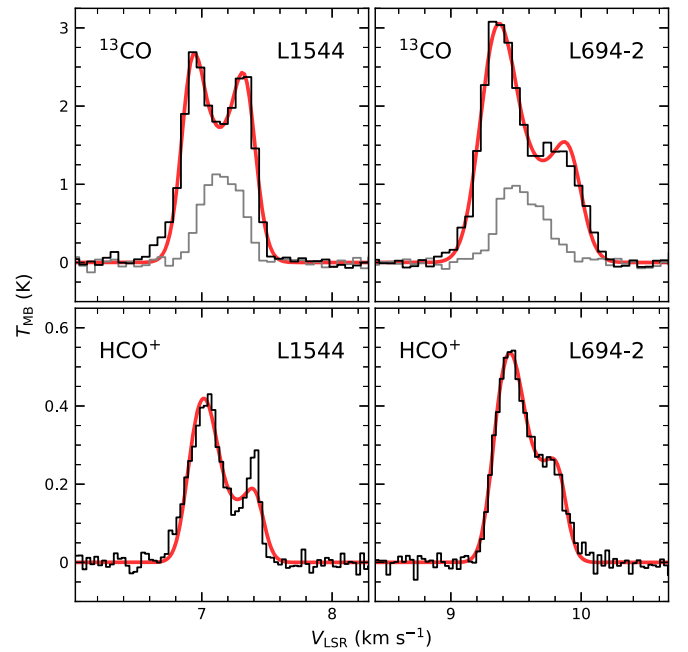
Figure 13. Infall asymmetric profiles of ^{13}CO (3–2) and HCO$^+$ (4–3) lines in L1544 (left panels) and L694-2 (right panels). The line profiles given here in black (^{13}CO and HCO$^+$) and gray (C^{18}O) were obtained by averaging the profiles within the 40% level contour of the peak H$_2$ column density (p_{40}) of each dense core. The red profiles are the best-fitted ones using the Hill5 model (De Vries & Myers 2005) for each average profile.

In the outer envelope of L694-2, assuming R_{in} as $r_{10} \sim 0.08$ pc, the mass infall rate is estimated to be 6.0 ± 0.8 $M_\odot$ Myr^{-1}. This indicates that the mass infall rates inside (from HCO$^+$ data) are fairly larger than the mass infall rates outside (from ^{13}CO data).

Considering the velocity difference (or infall velocity of $\sim$0.1 km s^{-1}) and the projected separation (or the infall radius of $\sim$0.04 pc) between the opposite sides of the contracting cores inferred from HCO$^+$ data in both target cores, the velocity gradient of both core regions to the line of sight would be about 2.5 km s^{-1} pc^{-1}, being about a factor of 2–6 larger than the velocity gradient of the filaments at the core boundary (discussed in the Section 5.1). Moreover, the estimated mass infall rates of the contracting motion of both cores are a factor of 5–6 greater than the mass accretion rate of the axial flow motion around the core. A core can grow initially by gaining mass from the axial flow motion along the filament. A sufficient accumulation of gaseous material around the core would lead to radial contraction of the dense core, helping the core to evolve. From the fact that L1544 and L694-2 are in a highly evolved state both chemically and kinematically (e.g., Crapsi et al. 2005; Keto et al. 2015; Kim et al. 2020), we can speculate that a significant amount of gaseous material has already been transported to these cores along the filament. In that sense, it is well explained why, in these targets, the amount of gas being accumulated by radial infall motions in the core region is presently more than from the axial flow motions along the filament at the core boundary.

### 6.2. Infall Motions in Filament Region

The previous section examined the infall motions around the high-density core regions. We note that similar infall motions can be also seen in the filamentary regions (Figure 14), analogous to the features reported in the low-density filamentary

Table 5
Mass Accretion by Infall Motions in Core Region

Target	Line	V_{in} (km s^{-1})	R_{in} (pc)	M_{in} ($M_\odot$)	$\dot{M}_{in}$ ($M_\odot$ Myr^{-1})
(1)	(2)	(3)	(4)	(5)	(6)
L1544	HCO$^+$ (4–3)	0.107 ± 0.008	0.044	2.2 ± 0.1	16 ± 2
L694-2	HCO$^+$ (4–3)	0.113 ± 0.015	0.038	1.4 ± 0.1	13 ± 3
L694-2	^{13}CO (3–2)	0.113 ± 0.004	0.081[a]	1.4±0.1	6 ± 1

Note. (1) Source name. (2) Transition. (3) Infall velocity derived by the Hill5 model fit. (4) Infall radius, r_{40}. (5) Mass calculated from the sum of H$_2$ column densities within the p_{40} contour. (6) Mass accretion rate by infall motion (mass infall rate).
[a] The infall radius is assumed to be r_{10} for ^{13}CO. See the text for details.
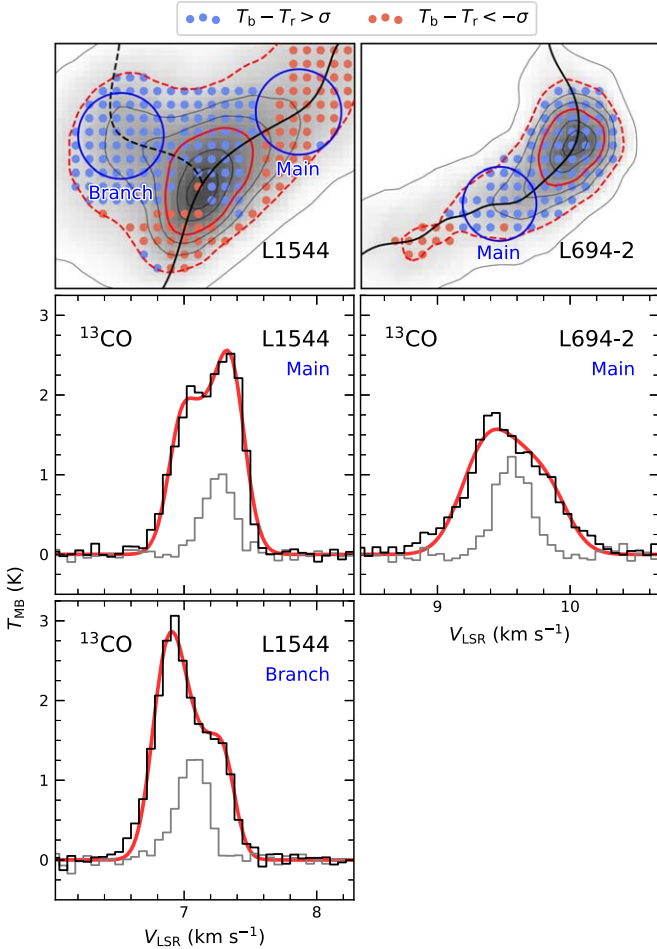
Figure 14. Line profiles of ^{13}CO (3–2) emission in the low-density filament region for L1544 (left panels) and L694-2 (right panels). Top panels: the blue and red dots indicate the pixel positions showing blue and red profiles of the ^{13}CO (3–2) line. The background gray tone and the overlaid contours show the H$_2$ column density distributions. The contours represent 80%, 60%, 40%, 30%, 20%, and 10% levels of the H$_2$ column peak density, and p_{40} and p_{10} levels are highlighted with the red solid and dashed contours (see Section 6.1). The blue circles mark the regions for averaging the profiles to create the ^{13}CO line profiles in the lower panels. Lower panels: the black and gray line profiles are the averaged ^{13}CO (Figures 20 and 21) and C^{18}O spectra, respectively. The red profiles show the best-fit results with the Hill5 model (De Vries & Myers 2005) for each averaged line profile.

clouds by, for example, Kirk et al. (2013) and Gong et al. (2018). In this case, the blue profiles of optically thick molecular lines were analyzed to infer the radial contraction toward the central axis of the filament. Then, assuming that the filament is a simple linear cylinder (see Figure 5 in Kirk et al. 2013), the mass accretion rate onto the filament in the radial direction can be calculated by

$$\dot{M}_\perp = \frac{2V_{in}M}{r\cos\alpha}, \qquad (8)$$

where V_{in} is the infall velocity, M is the filament mass, r is half of the filament width, and α is the inclination to the plane of the sky. The radial accretion rates onto the filament in the case of Serpens filaments were found to be much larger than the longitudinal mass accretion rates along the filament by a factor of 4–7 (Kirk et al. 2013; Gong et al. 2018).

The ^{13}CO data in this study also show the blue profiles (extended to the p_{10} level) indicative of the existence of inward motions in the filament region, not the core region. Figure 14 shows the line profiles of ^{13}CO averaged over regions of the branch filaments of L1544 and the main filament of L694-2. They are seen as blue profiles. Assuming that these blue profiles are due to the radial infall motions in the filament area in the same way as in Kirk et al. (2013), the infall velocities obtained by the Hill5 model fit are 0.11–0.13 km s^{-1} (corresponding to 0.15–0.18 km s^{-1} for a filament with an inclination angle of 45°), and the radial mass accretion rates onto the filaments are estimated to be about 6–7 $M_\odot$ Myr^{-1} (Table 6). This is a factor of 2 greater than the axial mass accretion rates along the filaments that we calculated in Section 4.2.

However, it is noted that we need to be careful in interpreting any asymmetric profiles from the periphery of the main filaments, especially if the filaments have a large velocity gradient along them. This is because the observed profiles may have some contribution from the axial flow motions that could modify the shapes of the asymmetric profiles (elaborated further in Appendix D). In fact, the line profiles in Figure 14 are averaged over a radius of 0.04 pc, and thus the radial velocity difference due to the velocity gradient within the area used for the averaging is about 0.1–0.2 km s^{-1}. Therefore, it is possible that the blue profile shapes in the branch part in L1544 and main part in L694-2 could be significantly affected by the axial flows along the filaments. The red profile shown in the main filament part of L1544 can be explained in a similar context. The profile is probably highly affected by the redshifted axial gas flow along the filament toward to the dense core region.

7. Discussion

In this study, we found that the surrounding material associated with the two prestellar cores has a filamentary structure (Section 4), the gaseous material is being accreted toward the cores along the quiescent filaments (Section 5), and the inner

Table 6
Mass Accretion by Infall Motions in Filament Regions

Target	Fil.	M_{area} $(M_\odot)$	$\langle\sigma_{tot}\rangle_{area}$ (km s^{-1})	α_{vir}	$V_\perp$ (km s^{-1})	$\dot{M}_\perp$ $(M_\odot\,\mathrm{Myr}^{-1})$
(1)	(2)	(3)	(4)	(5)	(6)	(7)
L1544	Main	0.73 ± 0.03	0.22 ± 0.05	1.9 ± 0.8	⋅	⋅
	Branch	0.82 ± 0.03	0.22 ± 0.04	1.6 ± 0.6	0.11 ± 0.01	7 ± 1
L694-2	Main	0.64 ± 0.04	0.22 ± 0.03	2.1 ± 0.6	0.13 ± 0.01	6 ± 1

Note. (1–2) Core and filament name. (3) Filament mass within the averaged area with radius of 0.04 pc for the line profiles in Figure 14. (4) Mean total velocity dispersion from C^{18}O observation. (5) Virial parameter, $\alpha_{vir} = 3\sigma_{tot}^2 R/GM$. (6) Infall velocity from the best fit for Hill5 model (De Vries & Myers 2005). (7) Mass accretion rate onto the filament (tan $\alpha \approx 45°$).

and outer envelopes are radially collapsing toward the core center (Section 6). The physical and kinematic characteristics of the filaments identified in L1544 and L694-2 are found to be consistent with those seen in filaments with embedded cores in the low-mass star-forming region (Hacar & Tafalla 2011). In particular, they have physical properties significantly similar to those of the small-scale, velocity-coherent filamentary structures, also called "fibers," found by decomposing techniques in turbulent large-scale filaments (e.g., Hacar et al. 2013; Chung et al. 2019).

7.1. Usefulness of Our Targets as Dense Cores Embedded in Isolated and Velocity-coherent Filaments

Decomposing velocity-coherent filaments in a filamentary cloud seen in continuum emission, which often contains multiple velocity components, is highly tedious and also complex to do. Complication in the decomposition has something to do with "multi-Gaussian decomposing" and the "friends-of-friends-in-velocity" method (Hacar et al. 2013; Chung et al. 2021) or the Dendrogram technique (Chung et al. 2019), which usually suffers from the ambiguities and uncertainties in getting the unique solution of decomposed components in the processes (e.g., Zamora-Avilés et al. 2017). Therefore, in the isolated filaments and embedded dense cores, a spatial variation of their velocity structures can be easily identified without any help of such challenging decomposing techniques. In that respect, L1544 and L694-2 could be suitable cases to study the role played by filamentary structures in the process of dense core formation.

7.2. Origin of Subsonic Characteristic

Prestellar/starless cores, including L1544 and L694-2, are generally subsonic (Lee et al. 1999; based on N$_2$H$^+$ (1–0) observations), and the velocity-coherent filaments around our target cores are also mostly subsonic (see Section 5.2). The quiescent internal motions in these filamentary clouds with coherent velocities are somewhat different from those seen in many turbulent filaments where the dense cores are forming (e.g., Chung et al. 2019, 2021). In the case of L1544 and L694-2, the subsonic characteristics of the dense cores seem to be inherited from the parent filaments. One explanation for this could be that at the stage of the formation of the filament, the gas flows collide and their turbulent motions are dissipated to form a quiescent filament at the earlier stage where individual dense core forms (André et al. 2014; Tafalla & Hacar 2015).

7.3. Core-forming Flow Motion along the Filament

The existence of the core-forming flow motion along the filament axis for our targets has been inferred from the $\lambda/4$ shift in the periodic variation of density and velocity distributions along the filamentary clouds (e.g., Hacar & Tafalla 2011; Hacar et al. 2022). Compared to the clear variation in the density distribution, the sinusoidal oscillations of the velocity field were relatively less pronounced in the previously reported cases (Hacar & Tafalla 2011; Liu et al. 2019) and also in the case of L694-2 in our study. However, the velocity oscillation found in the 0.5 pc-long main filament of L1544 was distinctly identified with double repetition of the redshift and the blueshift components (see Figure 8). In the first wavelength of the sinusoidal variation of the velocity distribution, it seems clear that there is a converging flow motion that can accumulate the gaseous material to form a central core. The formation of the dense core probably would produce more gravitational pull and then lead to more longitudinal contraction of the filamentary cloud to make the core evolve to a more condensed stage. On the other hand, it is noted that there is no corresponding density peak in the second wavelength of the velocity distribution in the northwest.

This is probably because the 1.3 $M_\odot$ Myr^{-1} mass accretion rate for this second part of the sinusoidal velocity pattern is significantly smaller than the 6.0 $M_\odot$ Myr^{-1} for the first part from the contributions of both main and branch filaments, and it may not be enough to form one more core at the second part of the sinusoidal in L1544. Another possible reason for the nonexistence of the secondary density peak would be that there is not enough material to form the other core at the edge of the filamentary cloud.

Such periodic velocity variation and gas motion parallel to the axis in the uniform density cylinder due to gravitational instability has been predicted in theoretical studies (e.g., Fiege & Pudritz 2000b). Gritschneder et al. (2017) showed that the initial geometrical bend of a filamentary cloud could initiate the core formation and produce the sinusoidal velocity oscillation feature like the first wavelength case of the velocity distribution in L1544. The initial geometrical perturbation can lead to a long-lived, stable oscillation until that filament becomes gravitationally unstable via a density enhancement.

7.4. Radially Contracting Core

In this study, we measured infall velocities of ~0.11 km s^{-1} in the inner region of both L1544 and L694-2 cores from HCO$^+$ (4–3) observations, which are consistent with those measured from N$_2$H$^+$ (1–0), DCO$^+$ (2–1) and (3–2), HCO$^+$ (3–2), o-H$_2$O (1$_{10}$–1$_{01}$), or o-NH$_3$ (1$_0$–0$_0$) observations in

previous studies (Williams et al. 1999, 2006; Caselli et al. 2012; Keown et al. 2016; Caselli et al. 2017). This suggests that, considering the high critical density of the HCO^+ (4–3) line, the gas is contracting even in the innermost, very dense regions ($n_{H_2} \gtrsim 10^6$ cm^{-3}) of these cores.

For the outer regions of cores, the infall velocity measured from the ^{13}CO (3–2) observations found to be similar to the ~0.11 km s^{-1} in L694-2. On the other hand, in the case of L1544, the infall asymmetry (blue profile) is not dominant, and thus the infall velocity is not very measurable in the outer region of the core, although there have been claims that there are infalling motions in L1544 cloud scales (e.g., Tafalla et al. 1998; Ching et al. 2022). This difference in the infall velocities of the outer region between L1544 and L694-2 cores is also consistent with the results obtained from CS (2–1) and (3–2) observations in Lee et al. (2001, 2004) showing the infall velocity of 0.02–0.03 km s^{-1} for L1544 and 0.07–0.09 km s^{-1} for L694-2. The velocity gradient indicative of the core-forming flow around the core is clearer in L1544 than L694-2. In contrast, the infalling motions in both inner and outer regions of the core are more clearly identified in L694-2. The outer region of the L1544 core seems to have more complex motions, probably due to the core-forming flow motion around the L1544 core as discussed in Section 7.3. For example, Lin et al. (2022) found from the observations with CH_3OH lines a feature implying an asymmetric accretion of material at the dust peak of L1544. Still, more observational studies are needed to determine the relationship between core-forming flow and contracting motion.

7.5. Possible Formation Mechanisms of Dense Cores and Filaments

Filament fragmentation by gravitational instability (e.g., Stodólkiewicz 1963; Inutsuka & Miyama 1997) is one of the essential core-formation mechanisms well supported by observations, such as the existence of the filaments in gravitational equilibrium and the chain of dense cores along the filaments with quasi-equal spacing (e.g., Tafalla & Hacar 2015). The sinusoidal velocity variation along the filaments found in this study can also be a feature that presents the core formation by filament fragmentation. In the final step of the "fray and fragment" scenario (Tafalla & Hacar 2015), dense cores are formed out of velocity-coherent fibers by gravitational instability, and in the resulting core chain, the inter-core distance is estimated to be approximately 0.2–0.3 pc. In the two clouds studied here, the filaments harbor only one core each, but the wavelength of velocity oscillation is about 0.2–0.3 pc (see Figure 8). In our case, the initial filament mass seems insufficient to make a series of multiple cores, but the velocity oscillation pattern is possibly a leftover signature of such fragmentation due to gravitational instability.

An alternative core-formation scenario is the shock-induced fragmentation, where turbulent flows collide to make shock-induced filamentary structures that in turn form dense cores from their fragmentation (Klessen et al. 2005). This scenario predicts a sharp physical transition of gaseous material over the filament, for example, a velocity variation and an increase in the velocity dispersion across the boundary of the filament as shown by Pineda et al. (2010).

We examined the ^{13}CO velocity centroid distribution for two target clouds in Figure 7, finding a large-scale velocity difference across both target clouds (see Section 5). In L1544, we also found a distinct increase of about 0.06 km s^{-1} in σ_{NT} of ^{13}CO across the filament boundary (see Figure 10). On the other hand, it is noted that the σ_{NT} increase across the filament in case of L694-2 is not as significant as L1544 considering its uncertainty and also that σ_{NT} lies in the subsonic regime over the whole filament region in both target cases. As discussed in Section 7.2, such a reduced σ_{NT} might be natural in these highly evolved systems in that turbulence dissipation can be sufficiently achieved. Therefore, our results seem to neither strongly support nor rule out core formation by shock-induced fragmentation.

In summary, the filamentary structure seen in the L1544 cloud might be the result of shock compression from the variations of the centroid velocity and the velocity dispersion across the filamentary cloud, and then the filament might contract gravitationally along the filament to form the cores. In the case of L694-2, there is no clear evidence showing that the shock-induced compression has occurred. But it is likely that the filamentary structure in the L1694-2 envelope cloud has experienced gravitational fragmentation to form its dense core L694-2.

8. Conclusion

We performed mapping observations in $C^{18}O$ (3–2), ^{13}CO (3–2), ^{12}CO (3–2), HCO^+ (4–3), and $H^{13}CO^+$ (4–3) emission lines with the JCMT radio telescope toward L1544 and L694-2 cores and their surrounding filamentary envelopes. By analyzing our molecular line observations and the Herschel continuum data, we have investigated how the mass accretes onto the prestellar cores embedded in the parsec-scale filamentary cloud in order to understand how the filamentary structures in the clouds play a critical role in the formation of the prestellar cores. H_2 column density and dust temperature were measured by the SED fitting procedure of the Herschel dust continuum data. Based on Gaussian fits to the $C^{18}O$ profiles (and also ^{13}CO profiles as an alternative method toward the low-density region where $C^{18}O$ is undetected), the velocity structure all along the skeleton of each filament was examined. The main results of this study are summarized below:

1. The $C^{18}O$ (3–2) line is found to be an optimal tracer of the kinematics of the filamentary structure around the prestellar core. The ^{13}CO (3–2) line was detected over the entire filamentary cloud until the H_2 column density goes down to 2×10^{20} cm^{-2}, and its line profiles in the high-density region show a feature of strong self-absorption. The ^{12}CO (3–2) line seems to be a poor tracer of kinematics in the filaments and the cores due to its very different distribution from those of ^{13}CO and $C^{18}O$ as well as its saturated features in the spectra due to its high optical depth. The infall asymmetries of the HCO^+ (4–3) line were significantly detected in the high-density core region.

2. To obtain a better estimate of the physical parameters of L1544 and L694-2, we determined more reliable distances for these two targets by identifying the distances where an abrupt jump in the stellar extinction occurs due to the existence of the clouds and cores using the Gaia DR2 parallax data and Pan-STARRS1 stellar photometry for M-dwarfs. The newly determined distances of L1544 and L694-2 are 175^{+4}_{-3} pc and 203^{+6}_{-7} pc, respectively.

3. We identified ∼0.5 pc-long filamentary structures that harbor the cores in both L1544 and L694-2. L1544 has another small filament branched out from the core. The identified filaments in both L1544 and L694-2 have physical properties comparable with the individual filamentary structures (so-called "fibers") composing the large-scale filaments as complex bundles. We found that the prestellar cores as well as the surrounding filamentary clouds are in a quiescent state in the sense that their nonthermal velocity dispersion is smaller than or equivalent to the sound speed of the gas. This may imply that the turbulence has already been dissipated during the forming processes of these quiescent structures.

4. The filaments in our two targets are velocity-coherent on a (sub)parsec scale, with velocity variations within a range of 0.3 km s^{-1} in the dense core size scale. The sinusoidal velocity oscillations with a $\lambda/4$ shift with respect to the oscillations of the column density distribution are seen in L1544 and L694-2, possibly indicating the core-forming flow motion along the axis of the filament. The mass accretion rates of these longitudinal flow motions are estimated as 2–3 $M_\odot$ Myr^{-1} with an assumption of the filament inclination of 45°, being comparable to the mass accretion rate for the Serpens cloud, but much smaller than those of the Hub filaments, cluster forming filaments, and high-mass star-forming IRDCs by 1 or 2 orders of magnitude.

5. Both the HCO$^+$ (4–3) and ^{13}CO (3–2) lines in the high-density core regions show strong self-absorption features, mostly seen as blue profiles, indicating that the gaseous material in both the surrounding envelope and the inner region of cores is infalling onto the core center. The infall velocities are measured to be about 0.1 km s^{-1} by the Hill5 model fit for both line profiles with the MCMC sampling technique. The mass infall rates are estimated as ∼16 $M_\odot$ Myr^{-1} for L1544 and ∼13 $M_\odot$ Myr^{-1} for L694-2 in the inner region of cores by HCO$^+$ spectra, and ∼6 $M_\odot$ Myr^{-1} in the outer envelope of L694-2 by ^{13}CO spectra. This may imply that the mass infall rates are higher inside than outside.

6. The ^{13}CO (3–2) lines show self-absorption features even in the filament region. In the main filament of L694-2 and in the branch filament of L1544, the averaged ^{13}CO lines show typical infall asymmetric features. Assuming these are due to the radial contracting of filaments, the radial mass accretion rates onto the filaments are estimated to about 6–7 $M_\odot$ Myr^{-1}. However, as the core-forming flow motion parallel to the filament axis can also contribute to the shapes of such asymmetric line profiles, interpreting the asymmetric profiles in the filaments where there exist gas flow motions along the filaments requires caution.

7. The filamentary clouds harboring two prestellar cores with coherent velocity structures are found to be an important laboratory to study the role of the filamentary structure of the clouds in the formation of dense cores. From this study we suggest that the filaments in our targets could be intermediate between a turbulent cloud and quiescent core that probably formed the shock compression of colliding clouds. The cores could then be formed by gravitational fragmentation of the filaments, and the continuing mass accretion through the filaments might lead the cores to evolve to the prestellar dense core

stage. We conclude that the filamentary structures in two clouds, L1544 and L694-2 consisting of dense cores, are likely playing a key role in the whole process of core formation and evolution.

Facilities: JCMT (HARP), Herschel (PACS, SPIRE).

Software: Starlink (Currie et al. 2014), Astropy (Astropy Collaboration et al. 2013, 2018), emcee (Foreman-Mackey et al. 2013), FilFinder (Koch & Rosolowsky 2015).

Appendix A
Estimation of H$_2$ Column Density and Dust Temperature

The H$_2$ column density and dust temperature were derived based on the SED fit using the Herschel dust continuum images from 160 (250 for L694-2) to 500 μm. The observed dust emission can be expressed by

$$I_\nu = B_\nu(T_d)(1 - e^{-\tau_\nu}), \tag{A1}$$

where $B_\nu(T)$ is the Planck function, T_d is the dust temperature, and τ_ν is an optical depth at the observing frequency ν, given as $\tau_\nu = \mu_{H_2} m_H \kappa_\nu N_{H_2}$. Here, μ_{H_2} is the mean molecular weight per hydrogen molecule (2.8; Kauffmann et al. 2008), m_H is the hydrogen atom mass, κ_ν is the dust opacity referred from OH5 (Ossenkopf & Henning 1994), and N_{H_2} is the H$_2$ column density.

The continuum image contains all of the emissions from the cloud components lying along the line of sight. Thus, the peak of the SED curve of the dense core could be shifted toward a shorter wavelength due to the fact that the low-density molecular gas in the large-scale molecular cloud has a relatively
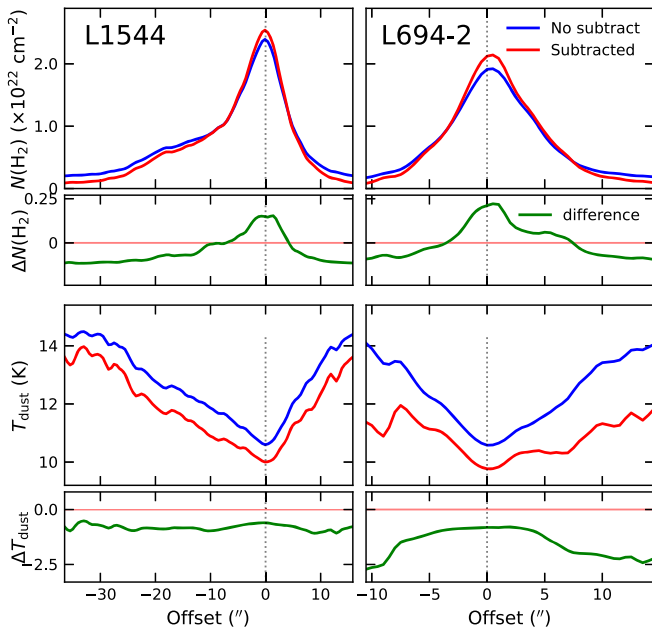
Figure 15. Effect of subtracting background emissions on L1544 (left panels) and L694-2 (right panels). The upper panels show the comparison for the H$_2$ column density profile along the cut in Figure 5 before (blue) and after (red) subtraction and their difference (green). The lower panels are the same, except for the dust temperature.

high temperature. Therefore, the background (or foreground, whichever it is) emission from such diffused gas should be subtracted before. Assuming that the background level is the mean intensity of pixels for which ^{13}CO was not detected, we measured the background levels as 23, 54, 34, and 15 MJy sr^{-1} for the Herschel 160, 250, 350, and 500 μm images, respectively. The determined background levels are similar to the dust emission at the H$_2$ column density of 1.1×10^{21} cm^{-2} with a dust temperature of 15 K. After subtracting the background, we also masked some pixels that have values lower than the rms noise level. The masking level is 1.8, 2.6, 1.9, and 0.9 MJy sr^{-1} for the 160, 250, 350, and 500 μm images.

Figure 15 shows the difference in SED fit results before and after background subtraction. Dust temperature was reduced by 1–2 K overall. Based on the boundary where the H$_2$ column density is approximately 10^{22} cm^{-2}, the H$_2$ column density decreased as some emission was removed in the low-density region but inversely increased in the high-density region due to the reduced temperature. As mentioned in Section 4, for the rest of the fitting procedure not described here, see Kim et al. (2020).

In the case of L694-2, we used only SPIRE 250, 350, and 500 μm data in the SED fit, because there is no PACS 160 μm

data in the Herschel science archive. However, we found that the differences between the two SED fit results for L1544 with and without 160 μm were quite negligible. Therefore, the absence of 160 μm data for L694-2 did not affect this SED fit result.

Appendix B
Distance Determination Based on Gaia DR2

We determined the distance of L1544 and L694-2 based on stellar photometry and Gaia DR2 parallax for the M-type dwarfs. The procedures are roughly split into two parts: (1) making the data set consisting of stellar optical extinction (A_v) and parallax distance, and (2) determining cloud distance by identifying where a sharp increase in extinction occurs.

The first part of the procedure refers to Maheswar et al. (2022, in preparation). To separate the M-type dwarfs in the Pan-STARRS catalog (Flewelling et al. 2020) into ON and OFF positions for the target cloud, we first set the cloud boundary to the 22 MJy sr^{-1} contour of the Planck 857 GHz image. The threshold was chosen arbitrarily to get the cloud region isolated from the ambient material. The ON-cloud stars can be separated again into the foreground and background stars for the target cloud. The background stars have relatively higher amounts of extinction than the foreground stars, and the extinction is sharply increased at the location of the target cloud. A baseline to correct for the normal interstellar reddening was identified from the distribution of OFF-cloud stars in the (g, r, i) color–color diagram. We dereddened ON-cloud stars using the baseline and obtained their extinction. Their parallax distances were procured from the Gaia DR2.

The fitting method refers to Yan et al. (2019), who derived the distance with Bayesian analysis and MCMC sampling from the extinction-distance data set. The likelihood model describing an extinction of a star is expressed by

$$p(A_{v\,i}|\mu_f, \sigma_f, \mu_b, \sigma_b, D) = f_i\,PF_i + (1 - f_i)\,PB_i, \qquad (B1)$$

where μ_f and σ_f are the extinction and its standard deviation of foreground stars, μ_b and σ_b for background stars, and D is the cloud distance. f_i and $(1 - f_i)$ are the probability of the star being in the foreground and background, respectively. PF_i and PB_i is the likelihood of measuring $A_{v\,i}$ for a foreground star and a background star, respectively.

The MCMC sampling was performed by using the emcee python package (Foreman-Mackey et al. 2013), and the sampling result is shown in Figure 16. The extinction change between foreground and background stars was about 1 mag in both targets. The best-fit values of cloud distance are 175^{+4}_{-3} pc for L1544 and 203^{+6}_{-7} pc for L694-2.
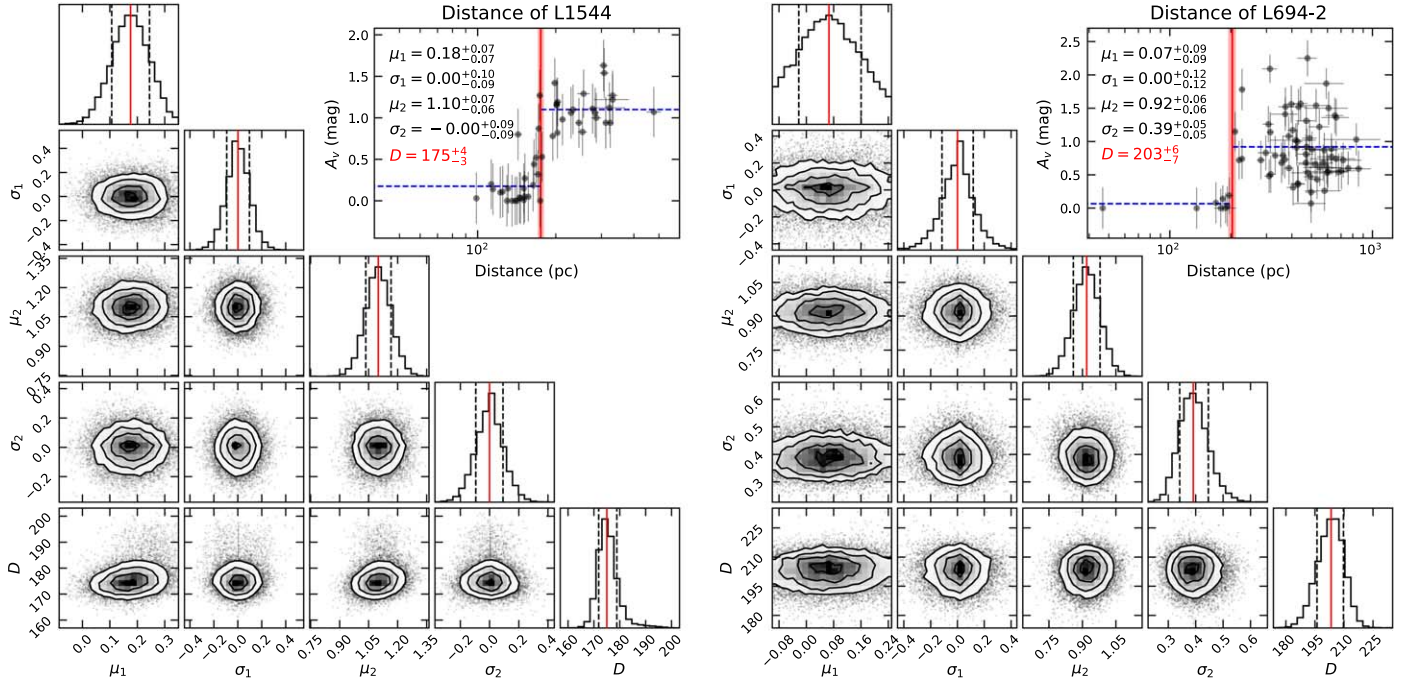
Figure 16. Determination of distances of L1544 (left panels) and L694-2 (right panels). The corner plots show the posterior probability distributions of parameters. The red lines show the median values of the parameters, and the dashed lines indicate the 16th and 84th percentiles of the parameters. The best-fit model and parameters are shown in the upper-right plot of each target (the units of μ and σ are magnitudes and D is in units of parsecs). The blue dashed lines show the extinction of foreground and background stars, and the red line and shaded area show the cloud distance and its uncertainty range.

Appendix C
Correction of Optical Depth Broadening

The observed velocity dispersion of an optically thick line such as ^{13}CO should be interpreted as a combination of optical depth broadening and intrinsic velocity dispersion of the gas (Hacar et al. 2016). The optical depth broadening, β_τ, is analytically defined as (Phillips et al. 1979),

$$\beta_\tau = \frac{\Delta V_{\rm obs}}{\Delta V_{\rm int}} = \frac{1}{\sqrt{\ln 2}}\left[\ln\left(\frac{\tau_0}{\ln\left(\frac{2}{\exp(\tau_0)+1}\right)}\right)\right]^{1/2}, \quad (C1)$$

where $\Delta V_{\rm int}$ is the intrinsic (or practically corrected) FWHM linewidth and τ_0 is central optical depth. To examine the optical depth broadening, the optical depth of ^{13}CO and C^{18}O lines should be determined. Using the isotopic ratio of C^{18}O and ^{13}CO in the local ISM (Wilson & Rood 1994), the optical depth of ^{13}CO can be calculated by multiplying the optical depth of C^{18}O and their isotopic ratio,

$$\tau_{13} \approx \tau_{18} \cdot X \approx 7.3\tau_{18}, \quad (C2)$$

where τ_{13} and τ_{18} are optical depths of ^{13}CO and C^{18}O, and X is the abundance ratio of ^{13}CO with respect to C^{18}O. The spectrum of a molecular line is represented by the radiative transfer equation (e.g., Wilson et al. 2013),

$$T_{\rm MB,\nu} = (J_\nu(T_{\rm ex}) - J_\nu(T_{\rm bg})) \cdot (1 - \exp(-\tau_\nu)), \quad (C3)$$

where $J_\nu(T_{\rm ex})$ and $J_\nu(T_{\rm bg})$ are the equivalent Rayleigh–Jeans excitation and background temperatures, and τ_ν is optical depth at frequency ν. The spectral optical depth, τ_ν, with Gaussian

distribution along the frequency is given as follows:

$$\tau_\nu = \tau_0 \cdot \exp\left(-(\nu - \nu_0)^2/2\sigma^2\right), \quad (C4)$$

where τ_0 is the peak optical depth at the central frequency ν_0, and σ is the intrinsic velocity dispersion. From the Equations (C2) and (C3), the line ratio of ^{13}CO and C^{18}O can be approximated by

$$\frac{T_{\rm MB}^{13}}{T_{\rm MB}^{18}} \approx \frac{1 - \exp(-\tau_{13})}{1 - \exp(-\tau_{18})} \approx \frac{1 - \exp(-\tau_{13})}{1 - \exp(-\tau_{13}/X)}, \quad (C5)$$

since the remaining term,

$$\frac{J_\nu^{13}(T_{\rm ex}) - J_\nu^{13}(T_{\rm bg})}{J_\nu^{18}(T_{\rm ex}) - J_\nu^{18}(T_{\rm bg})} \approx 1, \quad (C6)$$

only changes between 0.992 and 0.998 in the condition where $T_{\rm ex}$ is 5–20 K.

Figure 17 shows the median line profiles of ^{13}CO and C^{18}O emission, and their ratio. By fitting the model using Equation (C5) to this line ratio, τ_0 can be estimated. The best-fit values of τ_0 for ^{13}CO are 4.7 for L1544 and 7.4 for L694-2.

The ^{13}CO optical depth (τ_{13}) was determined by the method described above for all pixels where both ^{13}CO and C^{18}O were detected. Obtaining τ_{13} in the regions where C^{18}O was not detected is not straightforward, as the line ratio in those regions cannot be directly estimated. There are two possible ways to estimate τ_{13} for those regions, as shown in Figure 18: (1) by assuming the C^{18}O line intensity to be the 3σ noise level of the C^{18}O observation (the blue data points in the Figure), or (2) by extrapolating the relation between τ_{13} and $N({\rm H_2})$ obtained near the filament boundary regions (the dotted lines in the Figure). In the former case, the estimated τ_{13} rather increases at the lower column density regions because the ^{13}CO line is getting weaker
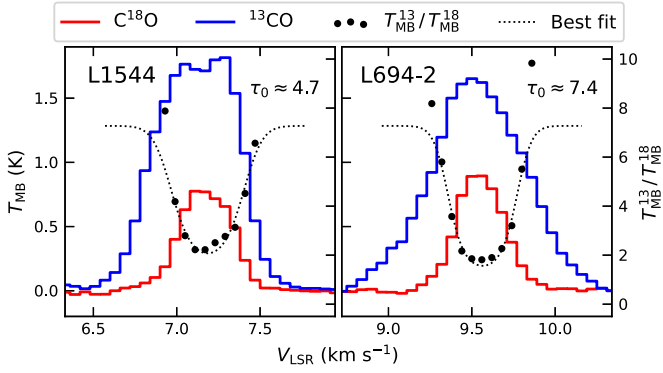
Figure 17. Median line profiles of ^{13}CO (blue) and C^{18}O (red) emission and their ratio (black points) in L1544 (left panel) and L694-2 (right panel). The dotted line is the best-fit model of the line ratios to derive the peak optical depth τ_0.
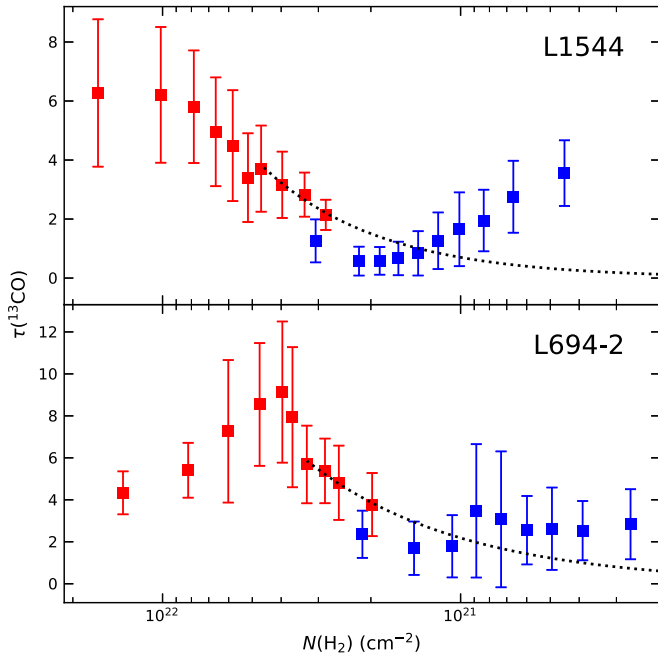
Figure 18. Variation of ^{13}CO optical depth with respect to H$_2$ column density. The optical depths are estimated from the line ratio of ^{13}CO and C^{18}O (red points). For the regions where C^{18}O was not detected, the optical depths were derived by assuming the C^{18}O brightness as the 3σ level of C^{18}O observation (blue points) or by extrapolating the relation between τ_{13} and N(H$_2$) obtained near the filament boundary regions to those low column density regions (dotted lines).

while C^{18}O intensity is fixed as the 3σ level. This would be different from the real situation. Therefore, we choose the latter method so that τ_{13} was estimated by extrapolating the relation between τ_{13} and N(H$_2$), which were obtained from the high N(H$_2$) regions ($2 \times 10^{21} < N$(H$_2$) $< 5 \times 10^{21}$ cm^{-2}) to the low N(H$_2$) regions where C^{18}O was not detected.

Figure 19 shows the results of correcting the optical depth broadening for the observed velocity dispersion. The optical depth broadening contributes 46% of the ^{13}CO linewidth at L1544 and 71% at L694-2 in the core and filament region. After correcting this, the nonthermal velocity dispersion of ^{13}CO was found to be mostly subsonic except for some regions outside the filament such as the northwestern end of the L1544 main filament (Figures 7 and 9).
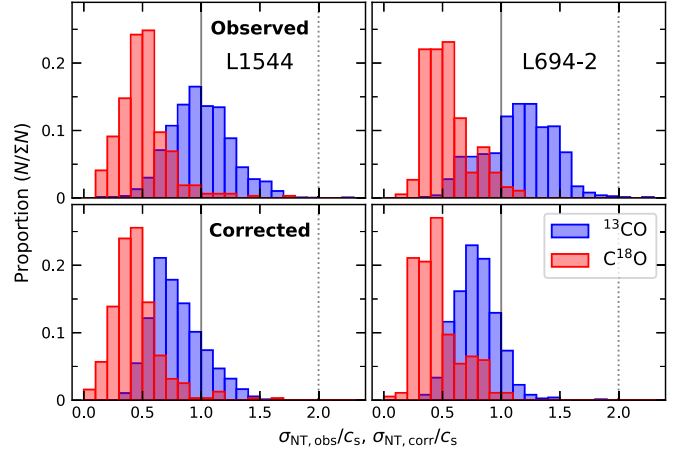
Figure 19. Histogram of nonthermal velocity dispersion expressed by Mach number for ^{13}CO (blue) and C^{18}O (red) lines in L1544 (left panels) and L694-2 (right panels). The upper panels show the distribution of observed nonthermal velocity dispersion, and the lower panels show the distribution of values corrected for optical depth broadening. The solid and dotted lines indicate the dividing lines among the sub-, trans-, and supersonic regimes.

Appendix D
^{13}CO Asymmetric Line Profiles

Figures 20 and 21 display the ^{13}CO line profiles in the surrounding filament region outside the core area shown in Figure 11, which are the original data of the blue and red profile distributions and averaged line profiles shown in Figure 14.

We discussed the ^{13}CO line profile in the filament region in Section 6.2. The blue- and redshifted components of the infall asymmetry detected near the prestellar core trace the motion of the contracting gas toward the core center. Similarly, we can also interpret the asymmetric line profile detected in low-density filaments as tracing the radial contraction motion toward the central axis of the filament. However, as we discussed in Section 6.2, there is a possibility that the longitudinal flow motion parallel to the filament axis, which is identified by the velocity gradient along the filament, could appear as such blue- and redshifted components in the line profile. Figure 22 displays a simplified model of a filament in the form of a linear cylinder. This is to help us understand the effects to the shapes of the asymmetric profiles due to the radial motions toward and longitudinal motions along the central axes of two types of filaments inclined in 45° to the sky plane: (a) a filament with a positive velocity gradient in the longitudinal gas motions and (b) a filament with a negative velocity gradient in the longitudinal gas motions.

The main filament of L1544 is characterized by a sinusoidal velocity oscillation being related to the core-forming flow (Section 5.1 and Figure 8). Accordingly, a decreasing velocity gradient appears near the positional offsets at about 0.1 and 0.3 pc along the filament, and Figure 22 (b) depicts this situation. In this case, both the radial infall motions onto the filament and the axial flow motions along the filament could appear as contracting gas motions to the line of sight and thus contribute to the shaping of an infall asymmetric profile.

On the other hand, Figure 22(a) is the other case where an increasing velocity gradient exists, and the axial flow motions appear as expanding motions, as seen near the positional offset of about 0.2 pc along the L1544 filament. This provides a possible explanation for the red profiles appearing near the position offset of 0.2 pc of the L1544 main filament (Figure 14).
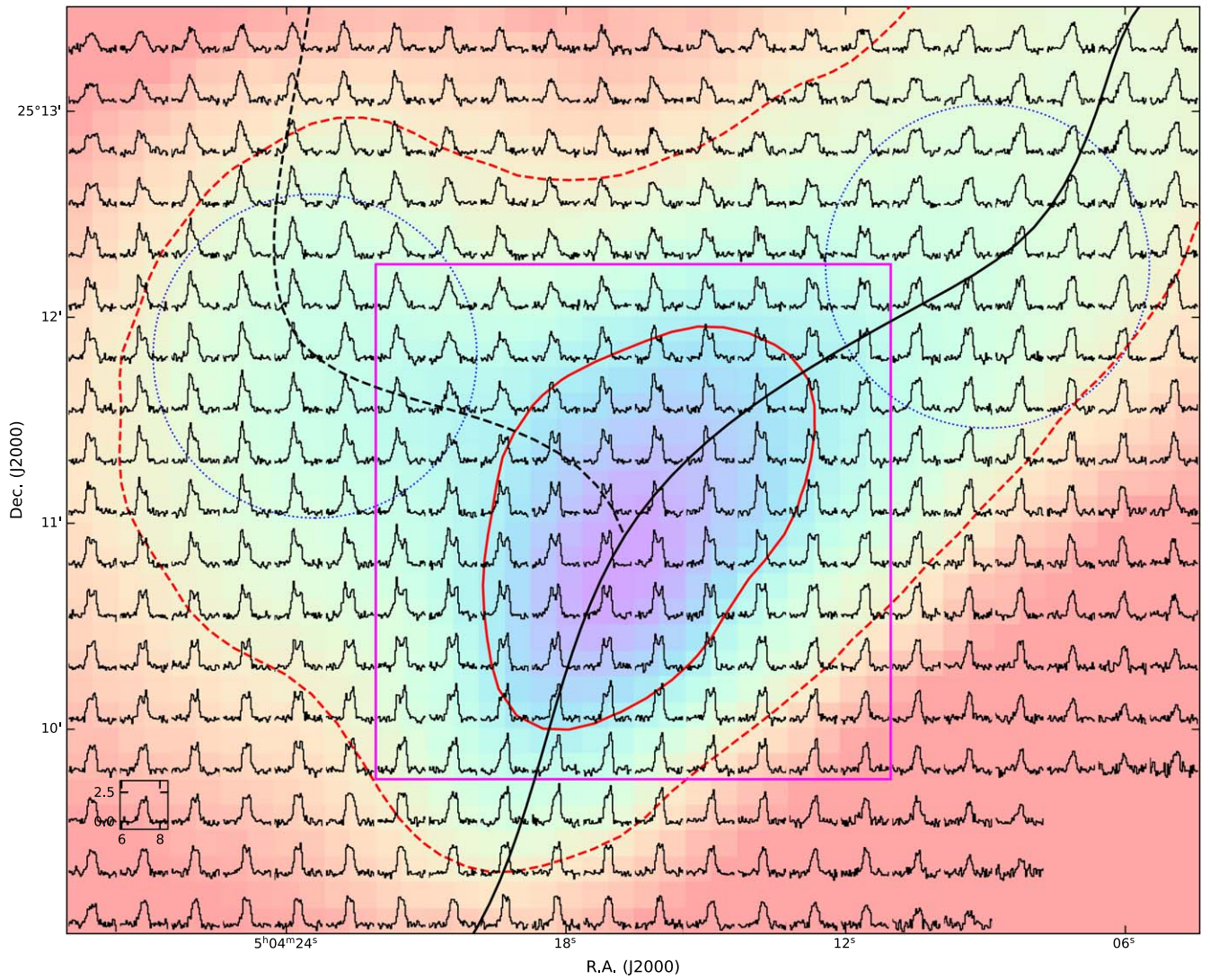
Figure 20. Line profile map of ^{13}CO (3–2) emission for L1544. The background colors show the H_2 column density distribution. The black solid and dashed lines are the skeletons of the filamentary structure. The red solid and dashed lines are contours with levels of p_{40} and p_{10}, respectively. The blue circles indicate the area where the averaged ^{13}CO and $C^{18}O$ line profiles of the filament region were obtained, as presented in Figure 14. The magenta square is to indicate the area of the ^{13}CO and HCO^+ line profile map in Figure 11.
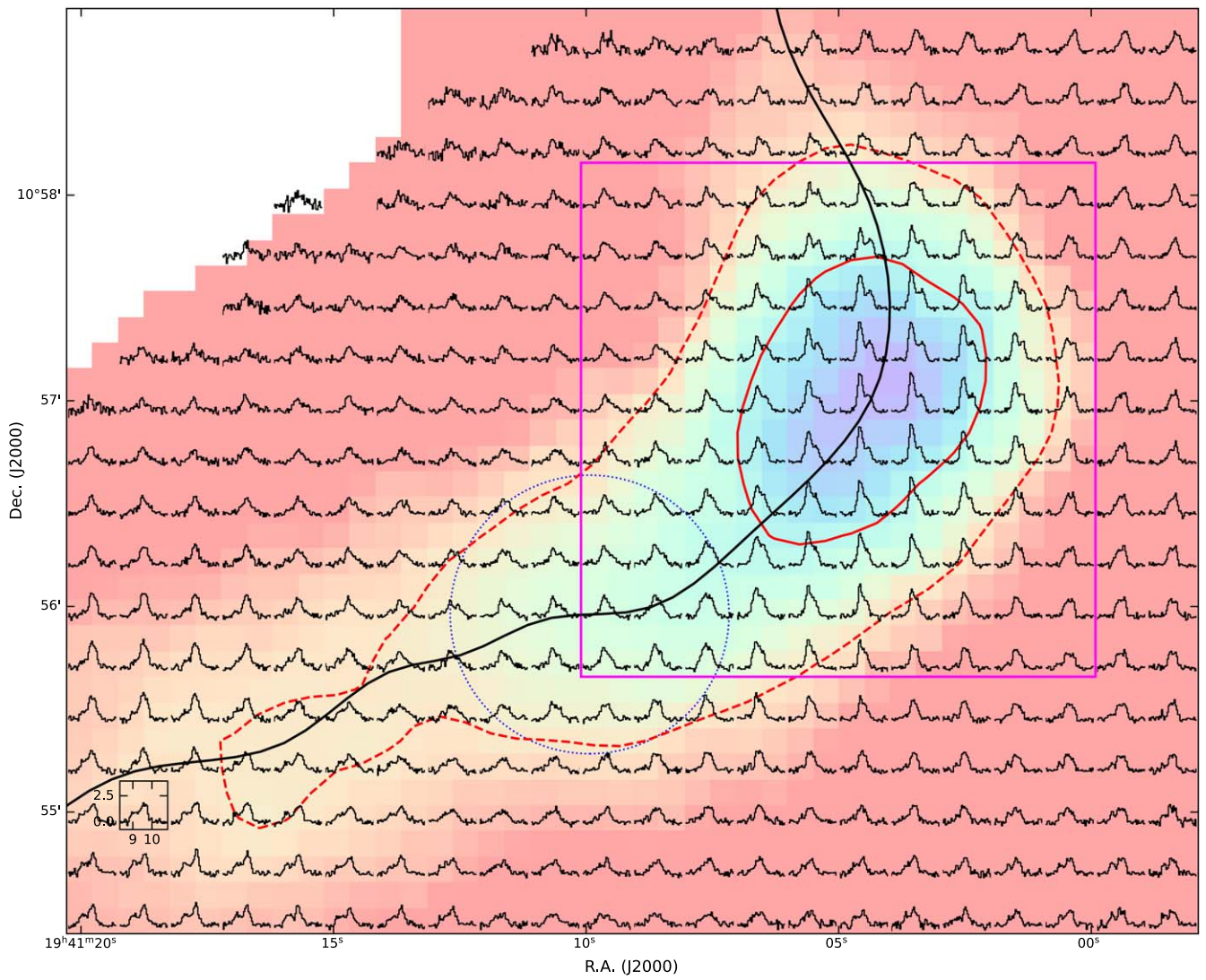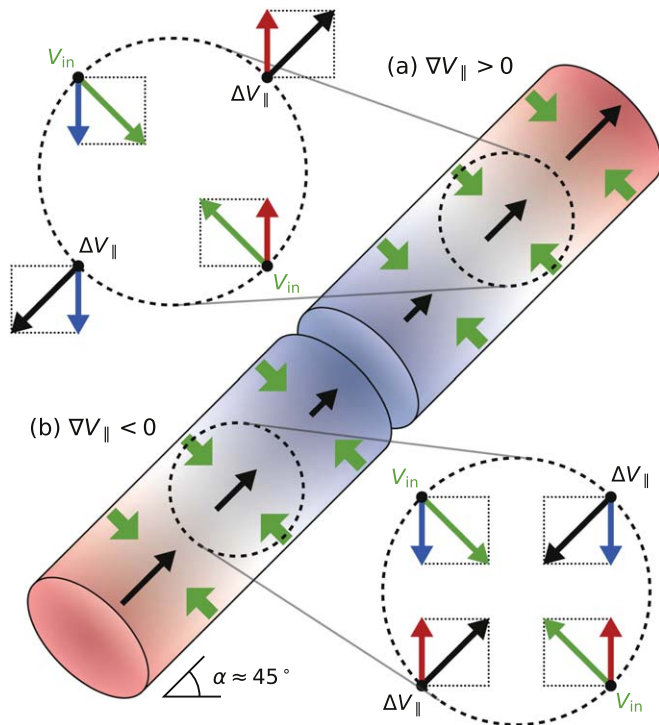
Figure 21. Same as Figure 20, but for L694-2.

Figure 22. Simplified model on the origin of the blue- and redshift motions detected in the filament with radial contracting motion and the large velocity gradient. The black arrows inside the cylinder and in the enlarged area indicate the velocity gradient along the filament and the axial velocity difference compared with the average velocity, respectively. The green arrows refer to the radial contraction motion of the filament. The blue and red arrows mean blue- and redshifted components, respectively, showing the observer's line-of-sight velocity components of axial motion and radial contraction in the area indicated by the dotted line. The dotted circle indicates the area of interest where the asymmetric profiles are considered.

ORCID iDs

Shinyoung Kim ⓘ https://orcid.org/0000-0001-9333-5608
Chang Won Lee ⓘ https://orcid.org/0000-0002-3179-6334
Mario Tafalla ⓘ https://orcid.org/0000-0002-2569-1253
Paola Caselli ⓘ https://orcid.org/0000-0003-1481-7911
Philip C. Myers ⓘ https://orcid.org/0000-0002-2885-1806
Eun Jung Chung ⓘ https://orcid.org/0000-0003-0014-1527
Shanghuo Li ⓘ https://orcid.org/0000-0003-1275-5251

References

André, P., Belloche, A., Motte, F., & Peretto, N. 2007, A&A, 472, 519
André, P., Di Francesco, J., Ward-Thompson, D., et al. 2014, in Protostars and Planets VI, ed. P. Beuther et al. (Tucson, AZ: Univ. of Arizona Press), 27
André, P., Men'shchikov, A., Bontemps, S., et al. 2010, A&A, 518, L102
Astropy Collaboration, Price-Whelan, A. M., Sipőcz, B. M., et al. 2018, AJ, 156, 123
Astropy Collaboration, Robitaille, T. P., Tollerud, E. J., et al. 2013, A&A, 558, A33
Benson, P. J., & Myers, P. C. 1989, ApJS, 71, 89
Bergin, E. A., & Tafalla, M. 2007, ARA&A, 45, 339
Buckle, J. V., Hills, R. E., Smith, H., et al. 2009, MNRAS, 399, 1026
Caselli, P., Bizzocchi, L., Keto, E., et al. 2017, A&A, 603, L1
Caselli, P., Keto, E., Bergin, E. A., et al. 2012, ApJL, 759, L37
Caselli, P., Walmsley, C. M., Tafalla, M., Dore, L., & Myers, P. C. 1999, ApJL, 523, L165
Caselli, P., Walmsley, C. M., Zucconi, A., et al. 2002a, ApJ, 565, 331
Caselli, P., Walmsley, C. M., Zucconi, A., et al. 2002b, ApJ, 565, 344
Ching, T.-C., Li, D., Heiles, C., et al. 2022, Natur, 601, 49
Chira, R.-A., Smith, R. J., Klessen, R. S., Stutz, A. M., & Shetty, R. 2014, MNRAS, 444, 874

Choudhury, S., Pineda, J. E., Caselli, P., et al. 2021, A&A, 648, A114
Chung, E. J., Lee, C. W., Kim, S., et al. 2019, ApJ, 877, 114
Chung, E. J., Lee, C. W., Kim, S., et al. 2021, ApJ, 919, 3
Clarke, S. D., Whitworth, A. P., & Hubber, D. A. 2016, MNRAS, 458, 319
Cox, A. N., & Pilachowski, C. A. 2000, PhT, 53, 77
Crapsi, A., Caselli, P., Walmsley, C. M., et al. 2005, ApJ, 619, 379
Crapsi, A., Caselli, P., Walmsley, M. C., & Tafalla, M. 2007, A&A, 470, 221
Currie, M. J., Berry, D. S., Jenness, T., et al. 2014, in ASP Conf. Ser. 485, Astronomical Data Analysis Software and Systems XXIII, ed. N. Manset & P. Forshay (San Francisco, CA: ASP), 391
De Vries, C. H., & Myers, P. C. 2005, ApJ, 620, 800
Dempsey, J. T., Friberg, P., Jenness, T., et al. 2013, MNRAS, 430, 2534
di Francesco, J., Evans, N. J. I., Caselli, P., et al. 2007, in Protostars and Planets V, ed. B. Reipurth, D. Jewitt, & K. Keil (Tucson, AZ: Univ. of Arizona Press), 17
Elias, J. H. 1978, ApJ, 224, 857
Endres, C. P., Schlemmer, S., Schilke, P., Stutzki, J., & Müller, H. S. P. 2016, JMoSp, 327, 95
Fiege, J. D., & Pudritz, R. E. 2000a, MNRAS, 311, 105
Fiege, J. D., & Pudritz, R. E. 2000b, MNRAS, 311, 85
Flewelling, H. A., Magnier, E. A., Chambers, K. C., et al. 2020, ApJS, 251, 7
Foreman-Mackey, D., Hogg, D. W., Lang, D., & Goodman, J. 2013, PASP, 125, 306
Gaia Collaboration 2018, Gaia Source Catalogue DR2, IPAC
Galli, D., Walmsley, M., & Gonçalves, J. 2002, A&A, 394, 275
Gong, Y., Li, G. X., Mao, R. Q., et al. 2018, A&A, 620, A62
Goodman, A. A., Barranco, J. A., Wilner, D. J., & Heyer, M. H. 1998, ApJ, 504, 223
Gregersen, E. M., Evans, N. J. I., Zhou, S., & Choi, M. 1997, ApJ, 484, 256
Gritschneder, M., Heigl, S., & Burkert, A. 2017, ApJ, 834, 202
Hacar, A., Clark, S., Heitsch, F., et al. 2022, arXiv:2203.09562
Hacar, A., Alves, J., Burkert, A., & Goldsmith, P. 2016, A&A, 591, A104
Hacar, A., & Tafalla, M. 2011, A&A, 533, A34
Hacar, A., Tafalla, M., Forbrich, J., et al. 2018, A&A, 610, A77
Hacar, A., Tafalla, M., Kauffmann, J., & Kovacs, A. 2013, A&A, 554, A55
Hennebelle, P. 2013, A&A, 556, A153
HGBS Team 2020, Herschel Gould Belt Survey, IPAC
Hirota, T., Ikeda, M., & Yamamoto, S. 2003, ApJ, 594, 859
HSA 2020, Herschel High Level Images, IPAC
Inutsuka, S.-i., & Miyama, S. M. 1997, ApJ, 480, 681
Jenness, T., Currie, M. J., Tilanus, R. P. J., et al. 2015, MNRAS, 453, 73
Kauffmann, J., Bertoldi, F., Bourke, T. L., Evans, N. J., & Lee, C. W. 2008, A&A, 487, 993
Kawamura, A., Kun, M., Onishi, T., et al. 2001, PASJ, 53, 1097
Keown, J., Schnee, S., Bourke, T. L., et al. 2016, ApJ, 833, 97
Keto, E., & Caselli, P. 2010, MNRAS, 402, 1625
Keto, E., Caselli, P., & Rawlings, J. 2015, MNRAS, 446, 3731
Kim, S., Lee, C. W., Gopinathan, M., et al. 2020, ApJ, 891, 169
Kirk, H., Myers, P. C., Bourke, T. L., et al. 2013, ApJ, 766, 115
Klessen, R. S., Ballesteros-Paredes, J., Vázquez-Semadeni, E., & Durán-Rojas, C. 2005, ApJ, 620, 786
Koch, E. W., & Rosolowsky, E. W. 2015, MNRAS, 452, 3435
Könyves, V., André, P., Men'shchikov, A., et al. 2015, A&A, 584, A91
Lai, S.-P., & Crutcher, R. M. 2000, ApJS, 128, 271
Lee, C. W., Kim, M.-R., Kim, G., et al. 2013a, ApJ, 777, 50
Lee, C. W., & Myers, P. C. 1999, ApJS, 123, 233
Lee, C. W., Myers, P. C., & Plume, R. 2004, ApJS, 153, 523
Lee, C. W., Myers, P. C., & Tafalla, M. 1999, ApJ, 526, 788
Lee, C. W., Myers, P. C., & Tafalla, M. 2001, ApJS, 136, 703
Lee, K., Looney, L. W., Schnee, S., & Li, Z.-Y. 2013b, ApJ, 772, 100
Li, S., Lu, X., Zhang, Q., et al. 2021, ApJL, 912, L7
Li, S., Sanhueza, P., Lee, C. W., et al. 2022, ApJ, 926, 165
Lin, Y., Spezzano, S., Sipilä, O., Vasyunin, A., & Caselli, P. 2022, A&A, 665, A131
Liu, H.-L., Stutz, A., & Yuan, J.-H. 2019, MNRAS, 487, 1259
Lu, X., Zhang, Q., Liu, H. B., et al. 2018, ApJ, 855, 9
Mouschovias, T. C. 1991, ApJ, 373, 169
Myers, P. C. 1983, ApJ, 270, 105
Myers, P. C., & Lazarian, A. 1998, ApJL, 507, L157
Ohashi, N., Lee, S. W., Wilner, D. J., & Hayashi, M. 1999, ApJL, 518, L41
Ossenkopf, V., & Henning, T. 1994, A&A, 291, 943
Ostriker, J. 1964, ApJ, 140, 1056
Padoan, P., Juvela, M., Goodman, A. A., & Nordlund, A. 2001, ApJ, 553, 227
Peretto, N., Fuller, G. A., Andre, P., et al. 2014, A&A, 561, A83
Phillips, T. G., Wannier, P. G., Scoville, N. Z., & Huggins, P. J. 1979, ApJ, 231, 720

Pineda, J. E., Goodman, A. A., Arce, H. G., et al. 2010, ApJL, 712, L116

Priestley, F. D., & Whitworth, A. P. 2020, MNRAS, 499, 3728

Rawlings, M. G. 2019, JCMT Users Meeting, Taipei, Taiwan, https://ftp.eao.hawaii.edu/jcmt/usersmeetings/2019-Taipei/Het_Calibration.pdf

Redaelli, E., Bizzocchi, L., Caselli, P., et al. 2019, A&A, 629, A15

Schneider, N., Csengeri, T., Klessen, R. S., et al. 2015, A&A, 578, A29

Shirley, Y. L. 2015, PASP, 127, 299

Shu, F. H., Adams, F. C., & Lizano, S. 1987, ARA&A, 25, 23

Sohn, J., Lee, C. W., Park, Y.-S., et al. 2007, ApJ, 664, 928

Stodólkiewicz, J. S. 1963, AcA, 13, 30

Tafalla, M., & Hacar, A. 2015, A&A, 574, A104

Tafalla, M., Mardones, D., Myers, P. C., et al. 1998, ApJ, 504, 900

Tafalla, M., Myers, P. C., Caselli, P., Walmsley, C. M., & Comito, C. 2002, ApJ, 569, 815

Valtchanov, I. 2017, SPIRE Products Explained, Release note, ESA, https://www.cosmos.esa.int/documents/12133/1035800/SPIRE+Products+Explained

Virtanen, P., Gommers, R., Oliphant, T. E., et al. 2020, NatMe, 17, 261

Ward-Thompson, D., André, P., Crutcher, R., et al. 2007, in Protostars and Planets V, ed. B. Reipurth, D. Jewitt, & K. Keil (Tucson, AZ: Univ. of Arizona Press), 33

White, G. J., Drabek-Maunder, E., Rosolowsky, E., et al. 2015, MNRAS, 447, 1996

Williams, G. M., Peretto, N., Avison, A., Duarte-Cabral, A., & Fuller, G. A. 2018, A&A, 613, A11

Williams, J. P., Lee, C. W., & Myers, P. C. 2006, ApJ, 636, 952

Williams, J. P., Myers, P. C., Wilner, D. J., & Di Francesco, J. 1999, ApJL, 513, L61

Wilson, T. L., Rohlfs, K., & Hüttemeister, S. 2013, Tools of Radio Astronomy (Berlin: Springer)

Wilson, T. L., & Rood, R. T. 1994, ARA&A, 32, 191

Yan, Q.-Z., Yang, J., Sun, Y., Su, Y., & Xu, Y. 2019, ApJ, 885, 19

Young, K. E., Lee, J.-E., Evans, et al. 2004, ApJ, 614, 252

Yuan, J., Li, J.-Z., Wu, Y., et al. 2018, ApJ, 852, 12

Zamora-Avilés, M., Ballesteros-Paredes, J., & Hartmann, L. W. 2017, MNRAS, 472, 647

Zucker, C., Speagle, J. S., Schlafly, E. F., et al. 2019, ApJ, 879, 125